

GROWING CRACK ANALYSES USING NODAL RELEASE TECHNIQUE

by

SUNGHWAN JUNG

B.S. in Mechanical Engineering
University of Iowa (1993)

Submitted to the Department
of Mechanical Engineering
in Partial Fulfillment of
the Requirements for the degree of

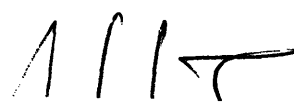
Master of Science in Mechanical Engineering

at the

MASSACHUSETTS INSTITUTE OF TECHNOLOGY

May, 1995

© Massachusetts Institute of Technology 1995



Signature of Author _____
Department of Mechanical Engineering
May 23, 1995

Certified by _____
David M. Parks
Professor of Mechanical Engineering
Thesis Supervisor

Accepted by _____
Ain A. Sonin
Departmental Committee on Graduate Studies

MASSACHUSETTS INSTITUTE
OF TECHNOLOGY

AUG 31 1995

LIBRARIES

Barker Eng

Growing Crack Analyses Using Nodal Release Technique

by

Sunghwan Jung

Submitted in partial fulfillment of the requirements for
the Degree of Master Science in Mechanical Engineering

Abstract

The objective of this work is to study plane strain fully-plastic crack growth behavior under pure extension in a non-hardening material using a FEM/continuum model. A nodal release technique is implemented in the elements on the symmetry line of a deeply-cracked single edge specimen so that the force at the crack-tip node on the symmetry line is made zero after several time steps upon the satisfaction of the chosen fracture criterion. The loading geometry-based crack-tip opening angle (CTOA), which McClintock, et al. (1994) proposed, is chosen as a fracture criterion for the growing crack.

First, the sensitivity of the results to the choice of mesh configuration is studied, and the results of the present model are compared to those of the line-spring model (Lee and Parks, 1994). Effects of deformation-induced geometry change on the crack-tip field and crack extension behavior are also intensively investigated.

Thesis Advisor: David M. Parks
Title: Professor of Mechanical Engineering

Acknowledgment

I wish to express my sincere gratitude to Professor David M. Parks for his enthusiasm, patience and insightful advice. I also wish to thank Professor Frank A. McClintock for providing many valuable comments.

I would also like to thank all the people in the Mechanics and Materials research group for their help in answering my questions. Specially I would like to thank Suryaprakash Ganti for his technical assistance.

I am greatly indebted to my parents. Without their constant support and encouragement, none of this would have been possible.

This work was supported by the office of Basic Energy Sciences, Department of Energy.

Table of Contents

TITLE PAGE	1
ABSTRACT	2
ACKNOWLEDGMENT	2
1. INTRODUCTION	5
1.1 Background.....	5
1.1.1 Parameter characterization of crack-tip field.....	5
1.1.2 Ductile fracture	9
1.2 Present work	10
2. CRACK GROWTH CRITERIA.....	13
2.1 Limitations of asymptotic solutions for growing crack.....	13
2.2 Sliding-off and Shear-cracking model.....	15
2.3 Least upper bound analyses	17
3. NUMERICAL IMPLEMENTATION	28
3.1 Symmetry boundary condition	28
3.2 Finite element formulation for the loading geometry-based CTOA	29
3.3 Nodal force relaxation at the crack-tip node	30
3.4 Crack growth simulation.....	32
4. RESULTS AND DISCUSSION	40
4.1 Method.....	40
4.2 Comparison with the line-spring model (Lee and Parks, 1994)	41
4.3 Crack growth simulations under pure extension.....	42
Appendix 4.1.....	49
5. CONCLUSION AND FUTURE WORK	75
5.1 Conclusion	75
5.2 Future work	76
REFERENCES.....	78

Chapter 1

Introduction

In this chapter, parameter characterizations of crack-tip field and micromechanisms of ductile fracture are reviewed. Also, the crack-tip opening angle parameter, which is adopted as the crack-growth criterion in the present work, is introduced. Then, the outline of present work is briefly stated.

1.1 Background

1.1.1 Parameter characterization of crack-tip field

Around 1950, singular crack-tip fields based on the stress intensity factor K were developed based on the theory of elasticity in order to describe the singular crack-tip fields. Under small-scale yielding, when the plastic zone is small compared to the characteristic dimension of the specimen, the single parameter K is useful to characterize the crack-tip field. This provides a fracture criterion for a brittle material, when small-scale yielding exists at the crack tip. When the stress intensity factor K determined from the loading condition reaches the critical value K_c , the crack begins to grow. However, if the structure being assessed is not sufficiently large compared to the annular region of K -dominance

around the crack-tip, the validity of the relation $K=K_c$ becomes questionable for predicting fracture of the structure. This limit of linear elastic fracture mechanics (LEFM) based on K provided the motivation for the study of elastic-plastic fracture mechanics.

Hutchinson (1968) and Rice and Rosengren (1968) independently derived the asymptotic crack-tip fields for a power law hardening material based on deformation theory of plasticity. They found that J can be used as a measure of deformation intensity by treating the response of power law hardening material to monotonic loading as that of a non-linear elastic material. At distances close to the crack-tip, elastic strains are negligible in magnitude compared to the plastic strains. In such case, the relationship between uniaxial strain ε and stress σ is expressible by

$$\frac{\varepsilon}{\varepsilon_y} = \alpha \left(\frac{\sigma}{\sigma_y} \right)^n, \quad (1.1)$$

where σ_y is tensile yield strength, ε_y ($=\sigma_y/E$) is the yield strain and E is Young's modulus; n is the strain hardening exponent, and α is a dimensionless parameter. J_2 -deformation theory of plasticity generalizes (1.1) to multiaxial states as

$$\frac{\varepsilon_{ij}}{\varepsilon_y} = \frac{3}{2} \alpha \left(\frac{\sigma_*}{\sigma_y} \right)^{n-1} \frac{s_{ij}}{\sigma_y}, \quad (1.2)$$

where s_{ij} is the deviatoric stress and $\sigma_* = \sqrt{3s_{ij}s_{ij}/2}$ is the equivalent Mises yield stress. Using the above constitutive relationship for the material, for a mathematically sharp, symmetrically loaded crack, the asymptotic expression of the crack-tip stress and strain fields (HRR field) in the region of small strains, can be obtained as

$$\sigma_{ij}(r, \theta) \rightarrow \sigma_y \left(\frac{J}{\alpha \varepsilon_y \sigma_y I_n r} \right)^{\frac{1}{n+1}} \tilde{\sigma}_{ij}(\theta, n) \equiv \sigma_{ij}^{HRR}, \quad (1.3)$$

$$\varepsilon_{ij}(r, \theta) \rightarrow \alpha \varepsilon_y \left(\frac{J}{\alpha \varepsilon_y \sigma_y I_n r} \right)^{\frac{n}{n+1}} \tilde{\varepsilon}_{ij}(\theta, n) \equiv \varepsilon_{ij}^{HRR}. \quad (1.4)$$

A normalization constant I_n and the dimensionless functions $\tilde{\varepsilon}_{ij}(\theta, n)$ and $\tilde{\sigma}_{ij}(\theta, n)$ depend on their argument(s), as shown in (1.3) and (1.4), and on whether either plane strain or plane stress is obtained at the crack tip. The J -integral is defined as the energy release rate in a nonlinear elastic body containing a crack and essentially measures the scale of crack-tip deformation. Considering Γ as any contour encircling the crack-tip in a counter-clockwise direction (Fig. 1.1), the line integral definition of J is

$$J = \int_{\Gamma} W dy - T_i \frac{\partial u_i}{\partial x} ds, \quad (1.5)$$

where W is the strain energy density, T_i are components of the traction vector acting outward on the contour, u_i are displacement vector components and ds is a length increment along the contour. Rice (1968) showed that the J -integral is path-independent if the material is homogeneous in the x -direction, with no body forces and traction-free crack faces. Under small scale yielding, J and K_I are related by

$$J = K_I^2 / E' \quad (1.6)$$

where $E' = E$ for plane stress, $E' = E / (1 - \nu^2)$ for plane strain; ν is Poisson's ratio. Similar to the crack initiation criterion associated with K , the parameter J , which can be calculated from the loading conditions (loading should be proportional for the deformation

theory to be valid), can be used for a crack initiation criterion. When the applied J equals the critical value J_c of the material, the crack begins to grow.

However, in shallow-cracked geometries, the loss of J -dominance at the crack-tip is observed (Al-Ani and Hancock, 1991). Hancock and co-workers argued that the loss of J -dominance results from the geometry-dependent non-singular constant stress term, the T -stress, in Williams' (1957) expansion series for the elastic field around a crack:

$$\sigma_{ij}(r, \theta) = \frac{K}{\sqrt{2\pi r}} f_{ij}(\theta) + T \delta_{ii} \delta_{jj}. \quad (1.7)$$

Initially, Larsson and Carlsson (1973) brought out the significance of the non-singular constant stress term in order to solve the crack-tip problem using a boundary layer approach (Rice, 1968). In their work, T -stress was observed to modify the shape of plastic zone size and to affect the crack-tip deformation. Bilby, et al (1986) also showed that negative T -stress substantially reduces crack-tip triaxiality (the ratio of the mean stress to the Mises stress at the crack-tip), which is a common measure of crack-tip constraint. J -dominance (when the local field is close to HRR field) implies that high crack-tip triaxiality is maintained in the crack-tip region. The T -stress, along with J -integral, can be used to describe the crack-tip fields under low triaxiality constraint (Betegón and Hancock, 1991).

However, J - T characterization is applicable only under well-contained yielding, and is formally undefined in fully yielded conditions. Therefore, for describing crack-tip fields in large-scale yielding, another two-parameter characterization J - Q was proposed by O'Dowd and Shih (1992). The second parameter Q represents a variation in hydrostatic stress from the reference field (either HRR or SSY solution), and it can be obtained by subtracting the reference field from the complete field obtained from highly refined finite element calculations. By observing full-field solutions, O'Dowd and Shih

(1992) showed that the Q -family of crack-tip fields exists for different crack geometries under large-scale yielding (O'Dowd and Shih, 1992).

1.1.2 Ductile fracture

Ductile materials are used for construction of pressure vessels and piping because their plastic behavior provides both warning before crack initiation and some amount of stable crack growth (Kim, et al., 1994a). In ductile materials, as a crack grows in a stable manner, a methodology accounting for stable growth of the crack as well as the crack initiation criterion, is needed. Crack initiation criteria can be obtained using a single or two parameter characterization and the material properties. However, for stable crack growth, crack-tip opening angle CTOA is believed to be a useful parameter to characterize the feature of stable crack growth (In elastic-plastic fracture mechanics, CTOA is ill-defined because of the elastic-strain singularity). The early stage of stable crack growth analyses associated with a local CTOA criterion are found in the works of Andersson (1973), Kanninen, et al. (1979), and Shih, et al. (1979). But, their computation of CTOA was somewhat arbitrary, without any physical basis.

Many workers found that crack growth in ductile material is a result of hole nucleation, growth and linkage in the region ahead of crack-tip (McClintock, et al., 1994), where elastic strains are usually negligible. Due to geometric constraint at the crack tip, triaxiality is usually high enough to nucleate holes, and the near-tip plasticity in ductile materials allows the holes to grow and link to the main crack-tip. Gurson (1977) proposed the widely-known micro-mechanical model for a porous ductile material, using averaging techniques similar to those of Bishop and Hill (1951). In his work, an aggregate of holes and rigid-plastic matrix material, rather than a polycrystalline aggregate, was considered as the characteristic volume element, and approximate upper-bound solutions on the micro-

level were used to derive a macroscopic yield condition for the material. This model has been applied to shear band localization between large scale holes. Tvergaard and Needleman, and many other workers applied the Gurson (1977) model to their computational models to investigate ductile crack growth. In the same spirit, a recent computational approach for ductile crack growth under large scale yielding can be found in the work of Lin, Shih, and Hutchinson (1994).

However, McClintock, et al. (1994) pointed out that if the ductile crack growth is only a result of micro-mechanisms of hole nucleation, hole growth, and hole linkage due in the shear band, the CTOA would only be a few degrees. Thus, they concluded that much of work related to fracture is spent in tearing between the irregular crack paths running up or down, due to planar localization or to fine cracks. From the observation of the zig-zagging feature of the cracked surface profile of ductile material, McClintock, et al. (1994) developed a sliding-off and shear-cracking model based on the near-tip plasticity and predicted CTOA in terms of the slip-line angle, normal stress, and shear displacement across the slip-line. Also, using limit analyses, they showed the strong dependence of CTOA on loading configurations. Furthermore, this development of the CTOA criterion motivated Kim, et al. (1994c), and Lee and Parks (1994b) to construct the line spring models for fully-plastic, plane strain crack growth simulations. A summary of CTOA-based fully-plastic crack growth developed by McClintock et al. is given in Chapter 2.

1.2 Present work

Several asymptotic solutions were suggested to characterize the crack tip field of stable crack growth in an ideally plastic solid under plane strain small scale yielding (Rice and Sorenson, 1978; Drugan, et al., 1982). However, when it comes to stable crack growth in low-strength alloys, the region of the of dominance of existing asymptotic

solutions is observed to be even smaller than the fracture process zone. Such limitations of the existing asymptotic solutions brought out the need for construction of a fully plastic plane strain stable crack growth criterion. McClintock, et al. (1994) proposed a crack-growth criterion in terms of CTOA from a sliding-off and shear-cracking model in order to account for fully plastic plane strain crack growth. Using upper bound limit analyses, they linked the value of CTOA to the given loading conditions so as to allow CTOA to evolve, depending on the loading geometry, during stable crack growth. Recently, Kim, et al. (1994c) and Lee and Parks (1994b) adopted the CTOA criterion to construct a line-spring model for the computational simulation of fully plastic crack growth in 3-D problems.

Here, in this work, the CTOA criterion is implemented in a 2-D plane strain FEM/continuum model of a deeply-cracked single edge specimen composed of an isotropic elastic/perfectly-plastic material. The main objectives of this work are to investigate both the macroscopic material responses and near-tip fields during fully plastic plane strain crack growth under pure extension. All the line spring model calculations (Lee and Parks, 1994b) show that final through-thickness penetration of high aspect ratio surface flaws in tension (shells are meant to be loaded in tension) occurs under essentially pure extension. In Chapter 2, the meso-mechanics of estimating CTOA from the sliding-off and shear-cracking model will be addressed, and the least upper bound approach method for determining crack-tip opening angle will be reviewed. In Chapter 3, numerical implementation of a nodal release technique will be discussed. In Chapter 4, numerical results using the FEM/continuum model will be presented, and the effects of material properties and geometric quantities on crack growth behavior will be discussed. Also, the results will be compared to those of the results of the line-spring model (Lee and Parks, 1994b) to verify the consistency of the two model formulations.

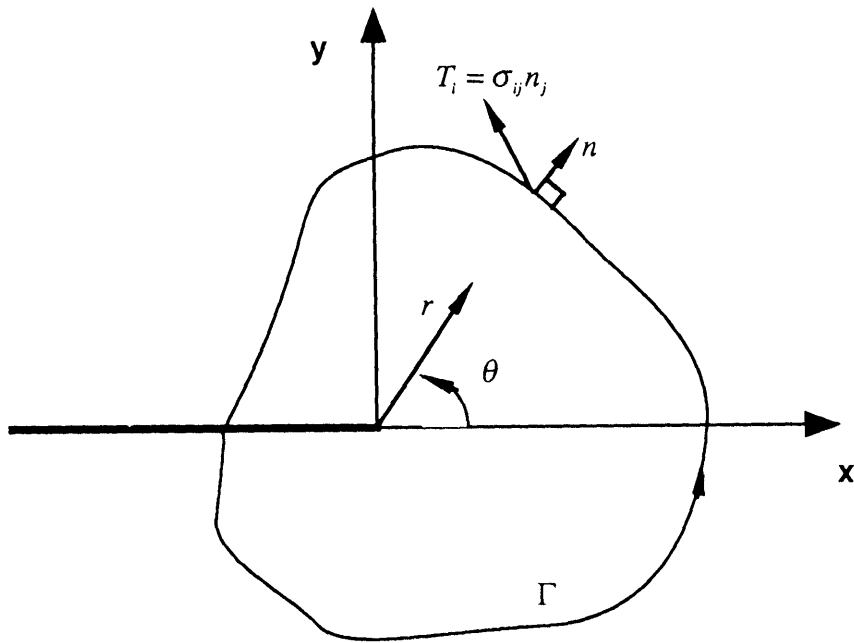


Fig. 1.1 The contour definition of J -integral.

CHAPTER 2

Crack Growth Criteria

In this chapter, the CTOA criterion, which is adopted in the present FEM/continuum model for fully-plastic crack-growth simulation, is discussed. First, limitations of existing asymptotic solutions for crack growth are investigated under fully plastic conditions. Then, a brief summary of the work for the development of the CTOA criterion for fully plastic crack growth is given, and the implementation of the criterion into our present model is discussed.

2.1 Limitations of asymptotic solutions for growing crack

Several asymptotic solutions were suggested to characterize the crack-tip field of stable crack growth in an ideally plastic solid under plane strain small scale yielding (Rice and Sorenson, 1978; Drugan, et al., 1982). Furthermore, Drugan and Chen (1989) introduced a family of asymptotic solutions, which can be applied even under large scale yielding and general yielding where the crack-tip triaxiality is much lower than small scale yielding. They also presented m -family of analytical solutions in order to predict the stress fields for different finite fully-yielded crack geometries (1991).

However, Gudmunson (1989) and McClintock, et al. (1994) found that the dominant region of existing asymptotic solutions for the fully-plastic plane strain crack growth of ductile material is much smaller than the fracture process zone. For example, for a growing crack under mode I, the equivalent strain ε^p at distance r in the crack-tip field can be approximated in terms of the tensile yield strain ε_y and the plastic zone size r_p (Drugan, et al., 1982):

$$\varepsilon^p \approx \varepsilon_y \ln(0.2r_p / r). \quad (2.1)$$

Replacing ε^p by the fracture strain ε_f , and then rearranging (2.1) provides a radius of dominance, r_d :

$$r_d = 0.2r_p \exp(-\varepsilon_f / \varepsilon_y). \quad (2.2)$$

For ductile, low strength materials, with a typical value of $\varepsilon_y \approx 0.002$, and even taking ε_f as low as $\varepsilon_f \approx 0.05$ under the assumption of high crack-tip stress triaxiality, and with a value of r_p as large as $r_p \approx 100\text{mm}$ under the assumption of fully-plastic yielding of a test specimen, McClintock, et al. (1994) found the value of, $r_d \approx 1.44 \times 10^{-5} \mu\text{m}$, which is so small as to be irrelevant to continuum aspects of ductile fracture. Such limitations of existing asymptotic solutions led to the construction of the loading geometry-based CTOA (McClintock, et al., 1994) for the fully-plastic plane strain crack growth of low-strength ductile material. Furthermore, the construction of the CTOA models motivated Kim et al. (1994c), and Lee and Parks (1994b) to independently develop line-spring models to simulate constraint-sensitive fully-plastic crack growth in 3-D. Our present FEM model also employs the loading geometry-based CTOA criterion as a fracture criterion in order to

simulate fully-plastic crack growth in plane strain. In the following sections, a brief summary of the work for the development of the CTOA criterion will be given, and the implementation of the criterion into our FEM model is also discussed.

2.2 Sliding-off and Shear-cracking model

Macroscopically straight crack growth is found to be a result of microscopic zig-zagging (McClintock, 1969; Carson, 1970; Tvergaard and Needleman, 1992). From this kind of feature of the crack path on the microscopic scale, McClintock et al. (1994) developed a sliding-off and shear-cracking model for fully-plastic, quasi-steady, plane strain crack growth in rigid/plastic non-hardening materials. Here, the sliding-off and shear-cracking model of McClintock, et al. (1994) is briefly reviewed.

In a sliding-off and shear-cracking model, the crack is assumed to grow in a zig-zag fashion, sliding off by s and cracking by c along a shear band before changing direction, as shown in Fig. 2.1. The geometry gives the form of CTOA in terms of slip line angle θ_s and s/c as

$$\tan\left(\frac{\text{CTOA}}{2}\right) = \frac{s \sin \theta_s}{(c + c + s) \cos \theta_s} = \frac{\tan \theta_s}{2(c/s) + 1}. \quad (2.3)$$

The total shear strain in the advancing shear band at fracture can be thought of as the sum of strains required to make holes initiate, grow and link to the form of micro-cracks. The width of the model shear band produced during one step of zig-zagging is $(s + c) \sin \theta_s$. Then the geometry gives the corresponding shear (fracture) strain, γ_f , as

$$\gamma_f = \frac{s}{(s + c) \sin 2\theta_s}. \quad (2.4)$$

Replacing (c/s) from (2.4) into (2.3) gives

$$\tan\left(\frac{\text{CTOA}}{2}\right) = \frac{\tan\theta_s}{2/(\gamma_f \sin\theta_s) - 1}. \quad (2.5)$$

The fracture strain depends on the mean normal stress across the slip-line at the crack tip and on the material properties. Accounting for hole nucleation and growth in a shear band, McClintock, et al. (1994) suggested a semi-empirical functional form for fracture strain γ_f as

$$\gamma_f = \frac{(1-1/n)A}{\sinh[(1-1/n)\sigma_s/\tau_o]} + B(\sigma_s) \quad (2.6)$$

where τ_o is the yield strength in shear, and n is the strain hardening exponent (plastic strain proportional to (stress) ^{n}). The dimensionless constant A and function $B(\sigma_s)$ are viewed as material properties considered to be determinable from fully plastic crack growth tests. The first term on the right hand side of (2.6) represents a strain for hole growth to linkage by micro-rupture, while the second term represents the strain for hole nucleation. Based on the model of hole growth in a shear band (McClintock, et al., 1969), the parameter A is related to the critical hole growth ratio at fracture by $A = 2\ln(R_f/R_o)$, where R_o is the initial hole size and R_f is the hole size at point of micro-localization between two grown holes. Fig. 2.2 shows the predicted inverse exponential dependence of the CTOA on σ_s/τ_o when a non-hardening ($n = \infty$) plane strain SEC specimen is subject to a flow field with $\theta_s = 45$ degrees. Typical values of A ranging from 0.2 to 1.2 in an increment of 0.2, were plotted, and no nucleation strain ($B(\sigma_s) = 0$) was assumed. Fig. 2.3 shows the dependence of the estimated CTOA on the slip-line angle for a non-hardening ($n = \infty$) material having $B(\sigma_s) = 0$ (McClintock, et al. 1995).

2.3 Least upper bound analyses

In a region of extensive plastic deformation, the elastic strain is small compared to the plastic strains and can be neglected. If strain hardening is also negligible, then the material can be idealized as a rigid-perfectly plastic material. In such a fully-plastic region, the slip-line theory provides an effective method to predict deformation and stress fields.

Although constructing the slip-line fields provides accurate solutions of the deformation fields in the fully plastic region, the slip-line field might not always be easy to construct. Therefore, in such cases it is attractive to estimate the upper limit load, which meets only the compatibility conditions and the given displacement boundary conditions. Kim, et al. (1994a) replaced the slip line field with one single arc based on kinematically admissible deformation fields and determined the least upper bound arc for a deeply-cracked single edge specimen where plastic deformation is constrained to the ligament for all loading conditions (Lee and Parks, 1993). Furthermore, for the deeply-cracked single edge specimen, these least upper bound analyses provide information on local crack-tip parameters such as crack-tip stress triaxiality and slip-line angle, which are useful in determining the CTOA. The predicted values of both global and local parameters solutions from the least upper bound (Kim, et al. 1994a) are found to agree well with the results of the FEM limit analyses by Lee and Parks (1993). Here, the least upper bound analyses for the deeply-cracked single-edge specimen of rigid/plastic non-hardening material under combined tension and bending are summarized (Kim, et al., 1994a).

First, three generalized forces such as shear force S , axial force N and bending moment M are introduced. When two of them are given, for example, S and N , and a kinematically admissible field as shown in Fig. 2.4 is applied, the upper bound theorem limits moment M as

$$M \leq \tau_o R^2 (\phi_2 - \phi_1) - N \left(\frac{t}{2} + L \right). \quad (2.7)$$

Here, $M + N(t/2 + L)$ is the moment about the origin O , and four kinematical variables (ϕ_1, ϕ_2, L, R) are subject to two kinematical constraints

$$\begin{aligned} L &= R \sin \phi_1, \\ L + l &= R \sin \phi_2 \end{aligned} \quad (2.8).$$

When ϕ_1 and ϕ_2 are selected as independent among the four kinematic variables, with the given upper bound solution, the least upper bound, can be obtained (McClintock, et al., 1994) by minimizing the right hand side of (2.7) with respect to ϕ_1 and ϕ_2 , and the solution of the least upper bound is described implicitly by the optimality conditions:

$$(\phi_2 - \phi_1) \cos \phi_1 - (\sin \phi_2 - \sin \phi_1) \left(\frac{1}{2} + \frac{N}{2\tau_o l} \sin \phi_2 \cos \phi_1 \right) = 0, \quad (2.9)$$

$$(\phi_2 - \phi_1) \cos \phi_2 - (\sin \phi_2 - \sin \phi_1) \left(\frac{1}{2} + \frac{N}{2\tau_o l} \sin \phi_1 \cos \phi_2 \right) = 0. \quad (2.10).$$

The normal component of the traction distribution along the optimized arc is assumed to satisfy Hencky's equilibrium equation such that

$$\sigma(\phi) = \sigma_r + 2\tau_o (\phi - \phi_r) \quad (2.11)$$

where the constant σ_r is the normal stress across the flow line at the reference point $\phi = \phi_r$ on the arc. If the normal stress $\sigma_r(\phi_r)$ is adjusted to equilibrate the shear force ($S = 0$), then the resulting traction distribution $\sigma(\phi)$ along the optimized arc (along with shear traction τ_o) also equilibrates both the other prescribed force, N , and the (unspecified) least

upper bound, M_{LUB} . Thus, all global equilibrium equations are satisfied by using the local stress field associated with the flow of the optimal kinematical field. The corresponding crack-tip normal stress σ_s and slip angle θ_s are given from Fig. 2.4:

$$\sigma_s = \sigma_r + 2\tau_o(\phi_2 - \phi_r); \quad \theta_s = \phi_2. \quad (2.12)$$

The loading parameter μ is introduced to measure the tension-to-bending ratio as

$$\mu = \frac{M + Na/2}{Nl}, \quad (2.13)$$

where $M + Na/2$ is the bending moment about the mid-ligament of the SEC specimen.

Using a small geometry change continuum finite element model composed of an isotropic elastic/plastic material obeying non-hardening J_2 flow theory of plasticity, Lee and Parks (1993) conducted limit analyses. The results were in good agreement with the simple estimates of θ_s and σ_s from 2.9 and 2.12 as well as the corresponding limit load state calculated from assumed tractions on least upper bound flow fields (Fig. 2.5, Fig. 2.6, Fig. 2.7).

Furthermore, McClintock, et al. (1994) extended the kinematically admissible field for the stationary crack under fully plastic conditions thus obtained to a fully plastic growing crack in order to relate the CTOA to the current loading (bending-to-tension ratio μ) during crack growth. This extension was made based on the following argument: Under fully plastic conditions, elastic strains are negligible so that the crack-tip field (stress-strain field) would be incrementally the same as for the stationary crack, and the plastic strain can be obtained by the superposition of the plastic strain increments with respect to the successive crack-tip positions. Therefore, following this argument, inserting the least upper bound solutions, σ_s and θ_s of (2.11) into (2.5) and (2.6) gives the

instantaneous CTOA in the fully plastic deeply-cracked SEC specimen as a function of current load ratio μ . Fig. 2.8 shows the predicted variation of CTOA with respect to μ in non-hardening plane strain single edge crack specimens for the values of $A = 0.2$ through 1.2 for $B(\sigma_c) = 0$.

In our FEM/continuum model, the tension-to-bending ratio μ is readily determined from symmetry plane nodal reactions. Here, σ_c and θ_c , which characterize the crack-tip fields, are assumed to be dependent on only μ in the manner as shown in Fig. 2.6 and 2.7. Then, the CTOA is determined through the relation as shown in Fig. 2.8. This macroscopic approach to CTOA accounts for the local aspects of the crack-tip fields indirectly through the current loading ratio μ . The coupling of deformation field with the nodal release is not taken into account in the present model formulation. Along with the loading geometry-based CTOA, a debonding algorithm is implemented into the elements on the expected crack-growth path. Upon the satisfaction of the local fracture criterion (the loading-geometry based CTOA), the nodal force at the crack tip is reduced to zero and the crack advances by one element-length.

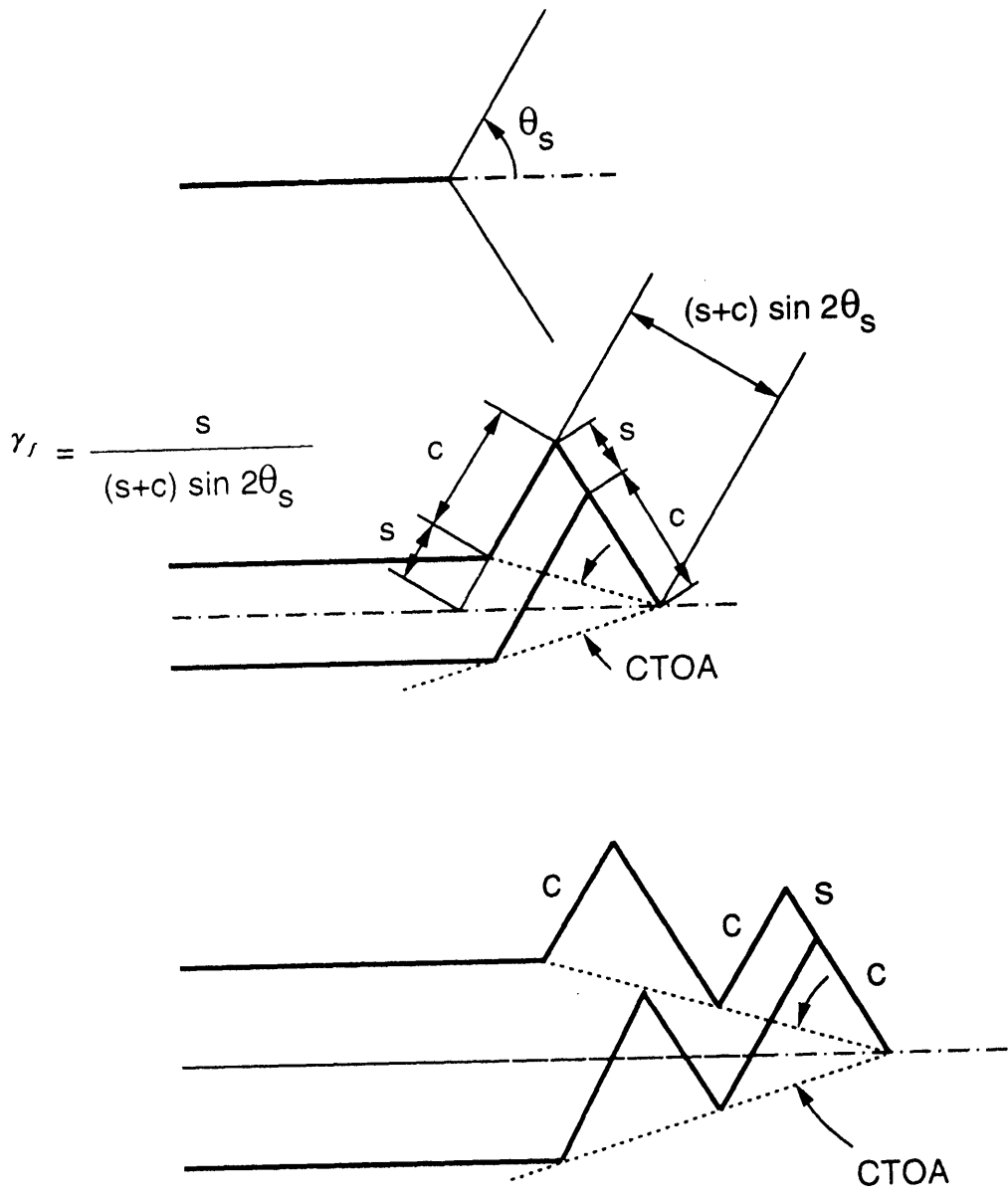


Fig. 2.1 Sliding-off and shear-cracking model for fully plastic, plane strain quasi-steady crack growth (McClintock, et al., 1994).

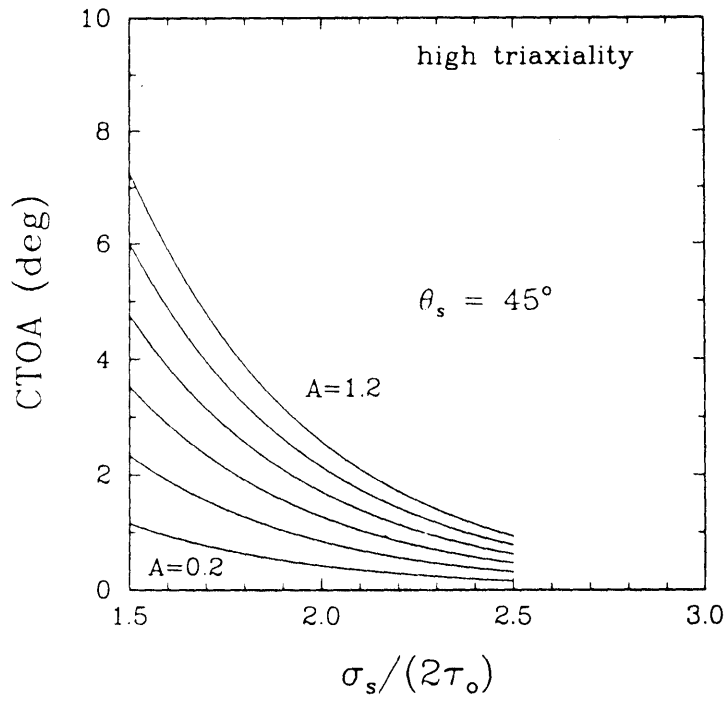
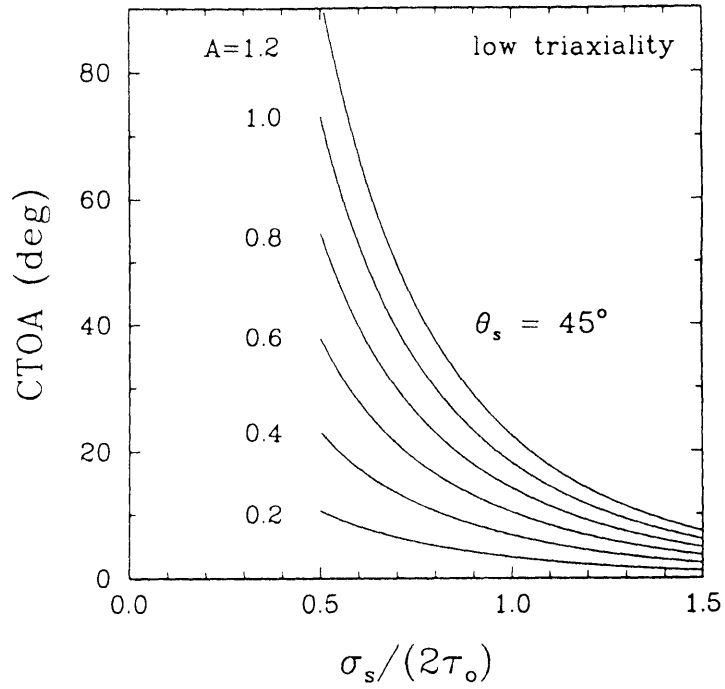


Fig. 2.2 CTOA vs. $\sigma_s/(2\tau_0)$ in a non-hardening material ($n = \infty$) for $\theta_s = 45^\circ$ and $B(\sigma_s) = 0$.

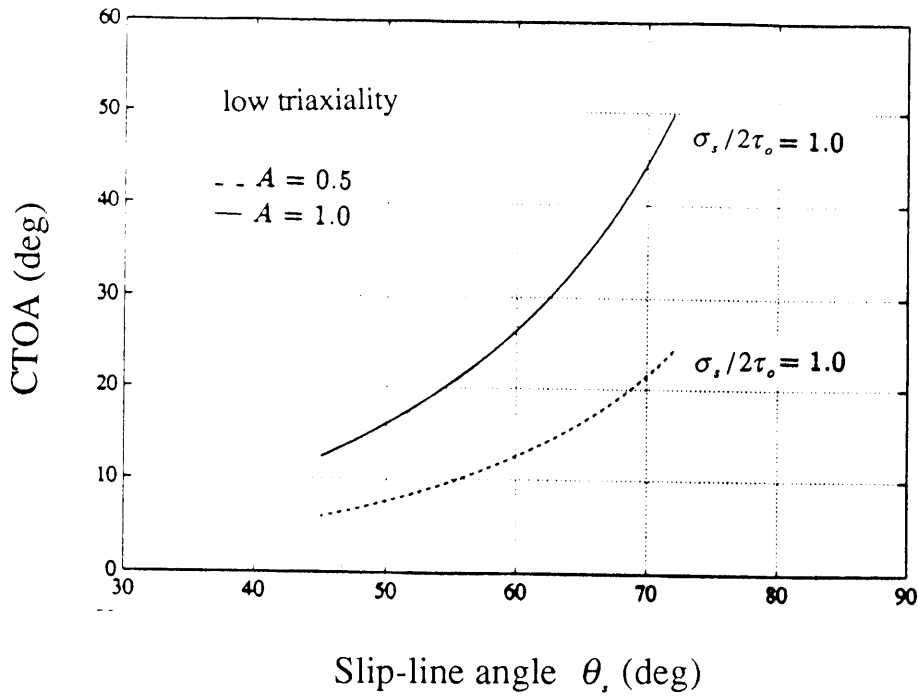
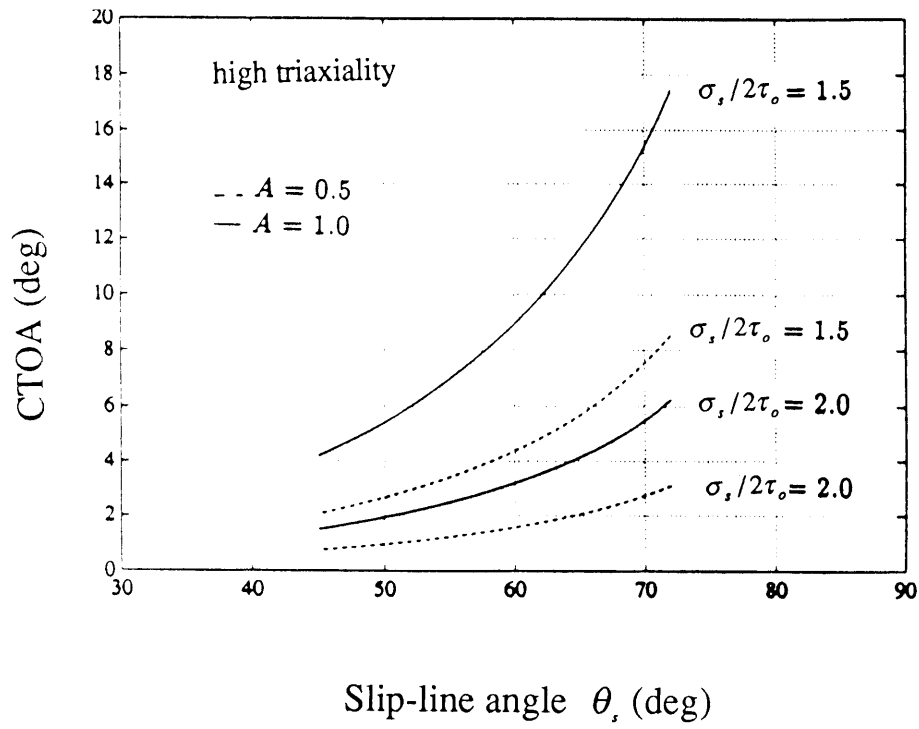


Fig. 2.3 CTOA vs. θ_s in a non-hardening material ($n = \infty$) for $B(\sigma_s) = 0$.

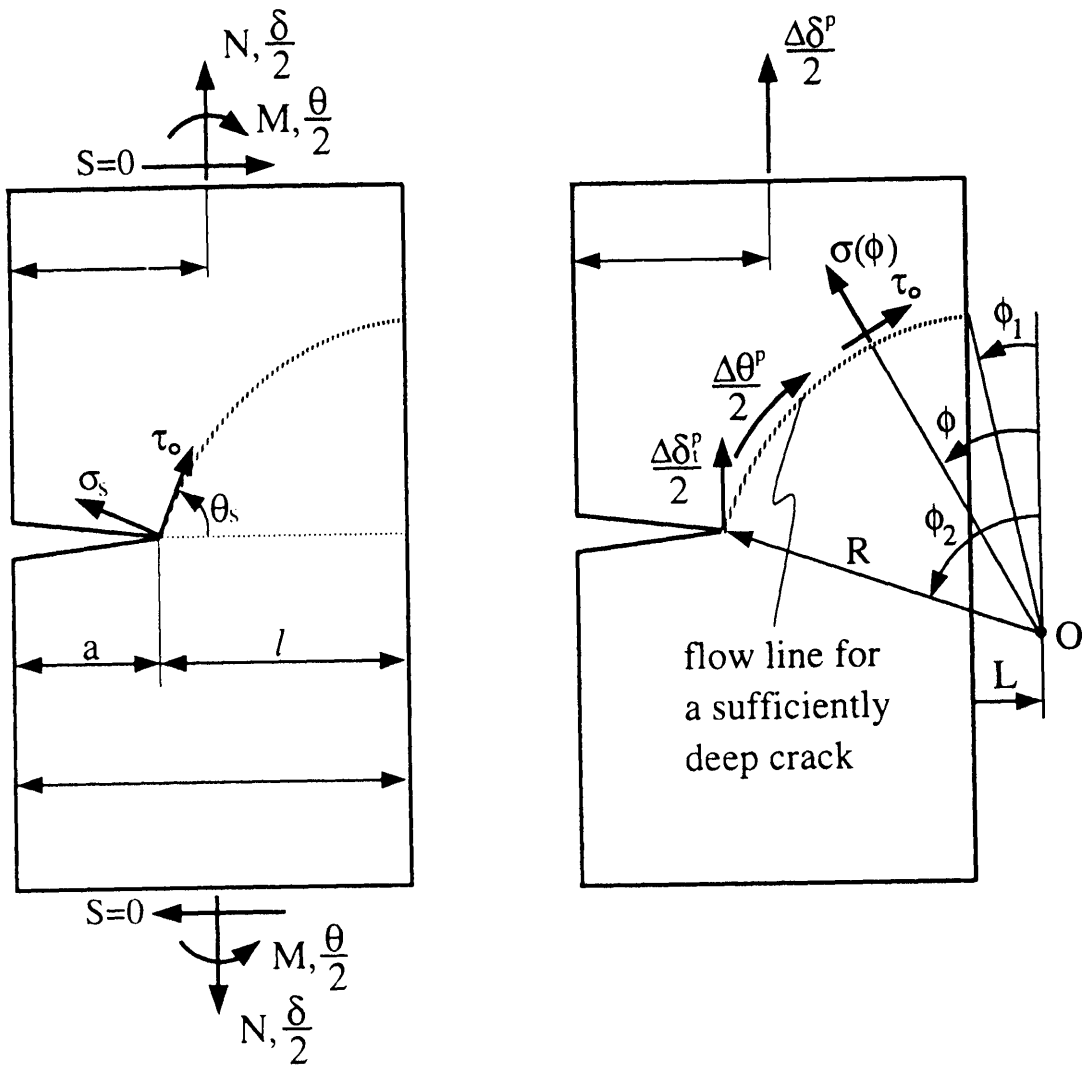


Fig. 2.4 Plane strain single edge specimen subject to combined tension and bending loading condition (left). Slip-line angle θ , and normal stress σ , across the flow line at the crack tip are also shown. Kinematically admissible field (right) used by Kim, et al. (1994a) to develop a least upper bound yield surface.

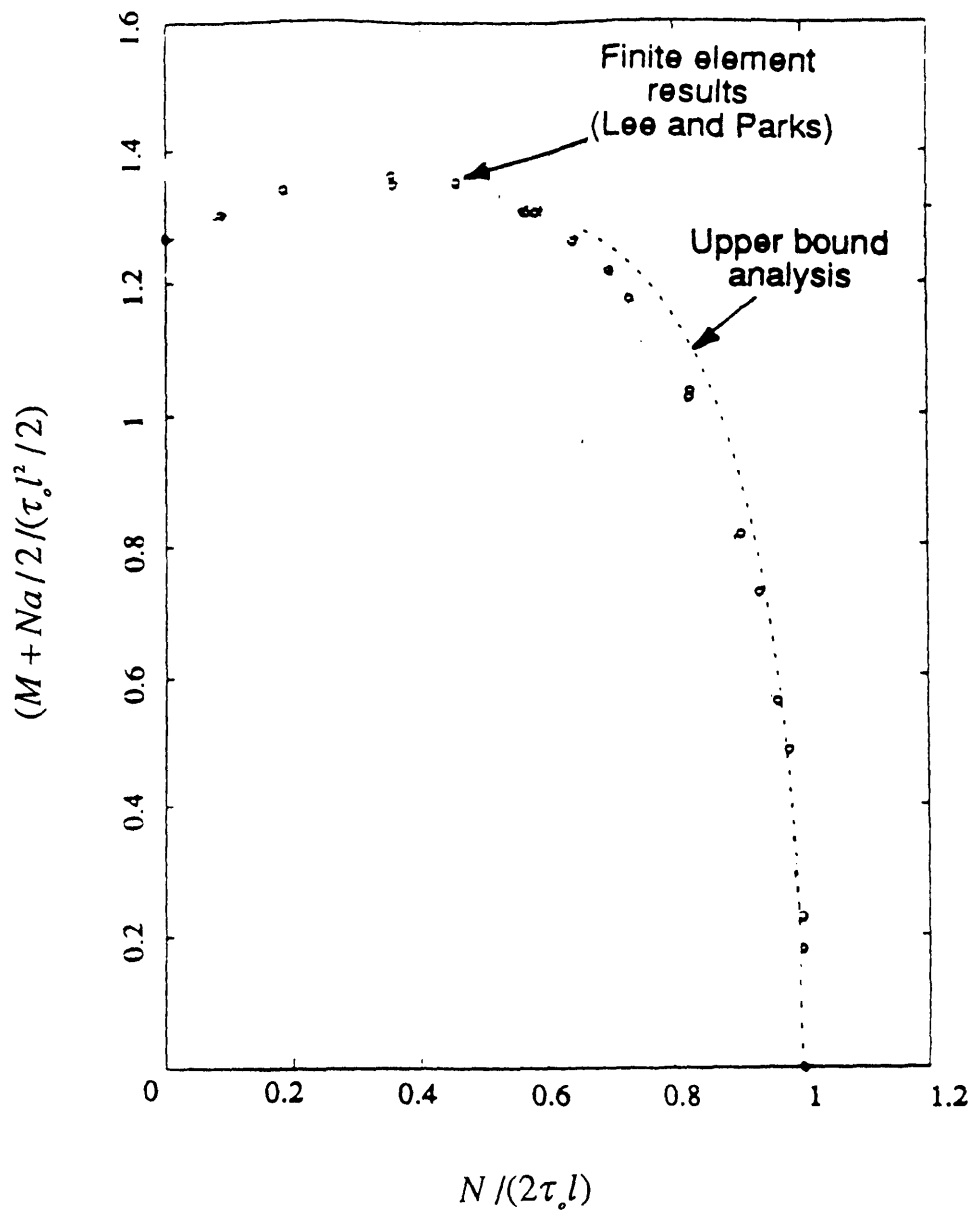


Fig. 2.5 Yield locus for a deeply-cracked single edge specimen subject to combined tension and bending.

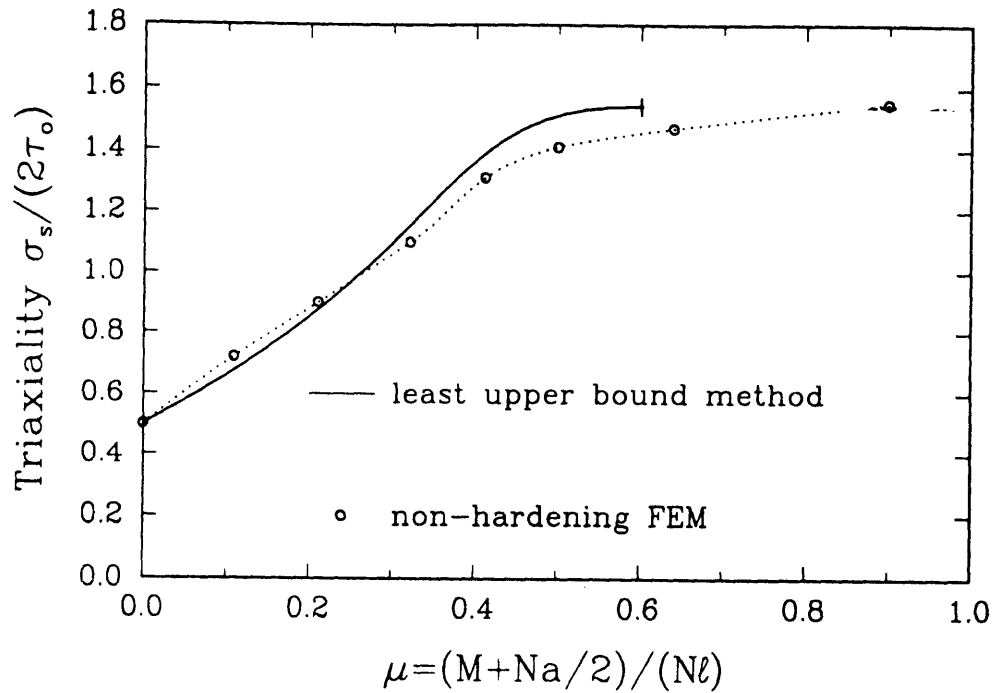


Fig. 2.6 Normal stress σ , across the flow line at the crack-tip of a deeply-cracked single edge specimen as a function of the loading ratio, μ .

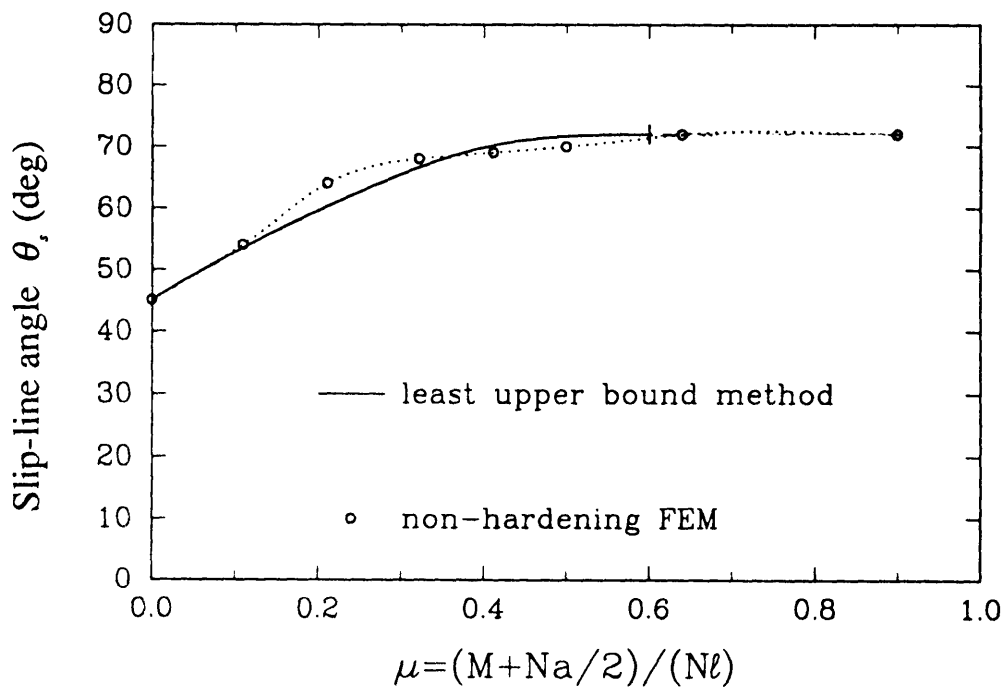


Fig. 2.7 Slip-line angle θ , at the crack-tip of a deeply-cracked single edge specimen as a function of μ .

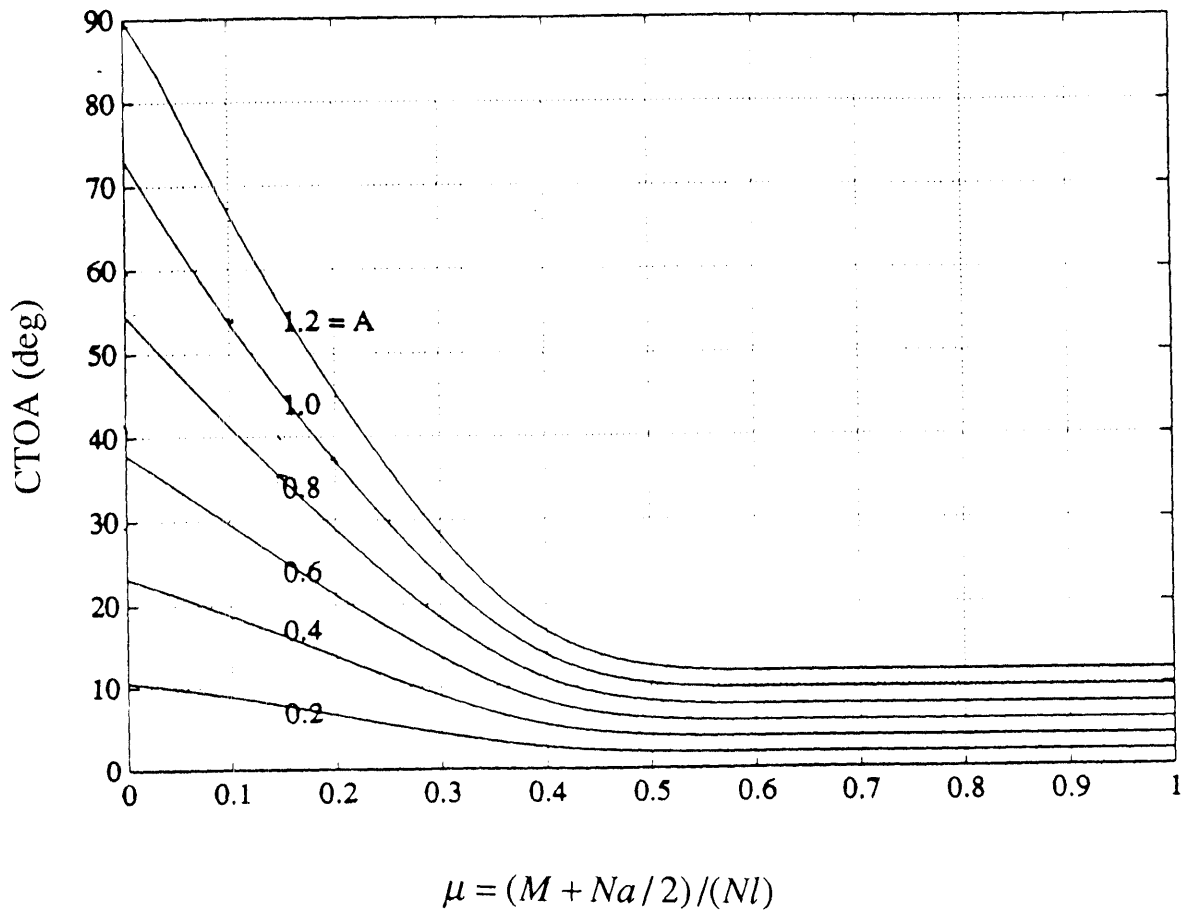


Fig. 2.8 CTOA vs. the loading ratio μ in a non-hardening ($n = \infty$) plane strain single edge specimen for $B(\sigma_r) = 0$.

Chapter 3

Numerical Implementation

A plane strain single edge specimen composed of an isotropic elastic/plastic material is modeled using a commercial finite element program (ABAQUS, HKS, 1994). Using symmetry arguments, only half of the specimen is considered in this work. The boundary conditions of combined displacement and rotation are imposed on the top edge of this finite element model as shown in Fig. 3.1. The magnitudes of the displacement and rotation at the loading point are made large enough to bring the material to fully yielded conditions.

Successive relaxation of the nodal forces at the node representing the crack tip is simulated in the main body of the ABAQUS finite element program.

3.1 Symmetry boundary condition

For the purpose of nodal release, a spring element is generated using the FORTRAN subroutine called UEL, which is available in ABAQUS. The spring element is connected to each node on the symmetry line of the uncracked part as shown in Fig. 3.2. The nodal stiffness ($=K_{22}$) of the spring element is initially specified to be much greater (about ten thousand times greater) than the uniaxial stiffness per unit thickness of one half of the specimen, which is given by

$$K_{specimen} = \frac{Ew}{L} \quad (3.1)$$

where E is Young's modulus of material, w is the width of the specimen, and L is the length of a half of the specimen. Therefore, the very high stiffness spring elements enforce the symmetry boundary condition by fixing the nodes on the symmetry line of the uncracked part due to such high stiffness. Once a chosen fracture criterion is satisfied at the node representing the crack-tip, the stiffness of the spring element connected to the crack-tip node is made zero, and the nodal force is reduced with increasing far-field displacement and rotation.

3.2 Finite element formulation for the loading geometry-based CTOA

The loading ratio, μ , is readily determined from the nodal reactions. Summing all the nodal reactions along the symmetry line gives the axial force N (Fig. 3.3) :

$$N = \sum_i F_i \quad (3.2)$$

where F_i is the nodal reaction at node i . The bending moment taken at the mid-ligament, M , is determined by

$$M = \sum_i F_i(x_i - l/2) \quad (3.3)$$

where x_i represents the distance of node i from the current crack-tip node and l represents the current ligament length. Then, the loading ratio μ is given as

$$\mu = \frac{M}{Nl}. \quad (3.4)$$

Finally the loading geometry-based CTOA, $CTOA(\mu)$, is determined with the relation shown in Fig. 2.8.

3.3 Nodal force relaxation at the crack-tip node

Upon the satisfaction of a chosen criterion, the reaction force corresponding to zero displacement at the crack-tip node is computed and relaxed to zero in several time increments as follows:

At the moment the fracture criterion is met, t_i , the crack tip is represented by node n . Using the local geometry at the crack-tip, at time t during debonding the force F_n at node n can be given as

$$F_n(t) = F_n(t_i) \left[1 - \frac{\delta_n(t)}{{}_c\delta_n} \right] \quad (3.5)$$

where $F_n(t_i)$ is the force at node n at time t_i when the chosen fracture criterion is met, δ_n is twice the relative displacement of node n from the symmetry line at time t (Fig. 3.4), and ${}_c\delta_n$ is the corresponding value of δ_n when F_n reaches zero. The parameter ${}_c\delta_n$ is determined as

$${}_c\delta_n = 2\Delta a^n \tan(CTOA(\mu(t_i)/2)) \quad (3.6)$$

where Δa^n is the length along the crack direction of the element directly ahead of the currently-releasing node n (Fig. 3.4). The CTOA is computed at the time t_i , (with (3.2), (3.3), and (3.4)), and is kept constant during debonding of node n .

Unfortunately, we were unable to implement the debonding curve of (3.5) associated with δ_n , in the present model, due to numerical difficulties. Thus, to avoid the difficulties, the force at the crack-tip node is taken to depend on the far-field geometry; i.e., it is decreased with far-field displacement and rotation. Also, for consistency with the local CTOA criterion, δ_n is estimated with the total far-field displacement ($=\delta$) and total rotation ($=\theta$) (Fig. 3.1), using the kinematic relationship which Lee and Parks (1993) proposed in the fully plastic regime. The plastic part of δ_n ($=\delta_n^{(p)}$) can be related to the load point plastic displacement ($=\delta^{(p)}$) and plastic rotation ($=\theta^{(p)}$) in incremental form as

$$\Delta \delta_n^{(p)} = \Delta \delta^{(p)} \left[1 + L_2 \cdot \left(\frac{1}{2} - \frac{a}{w} \right) \cdot \left(\frac{w \Delta \theta^{(p)}}{\Delta \delta^{(p)}} \right) \right] \quad (3.7)$$

where a/w is the instantaneous relative crack depth, and $\Delta \delta^{(p)} / (t \Delta \theta^{(p)})$ is the ratio of the load-point plastic displacement increment to the plastic rotation increment multiplied by the single edge crack specimen thickness. In the case of the single edge deep-crack specimen ($a/w > 0.35$), L_2 , which represents the degree of negative relative rotation of the crack flank with respect to the far field rotation, is unity. Since the specimen is in the fully plastic regime, the elastic part of δ_n and elastic parts of δ and θ can be neglected ($\delta_n \approx \delta_n^{(p)}$, $\delta \approx \delta^{(p)}$ and $\theta \approx \theta^{(p)}$). Therefore, in the present model, replacing δ_n with the far-field displacement ($=\delta$) and rotation ($=\theta$), the force F_n is given at time t as

$$F_n(t) = F_n(t_i) \left[1 - \left(\frac{1}{\delta_n} \right) \cdot \left(f \cdot \int_{\delta(t_i)}^{\delta(t)} \left[1 + L_2 \cdot \left(\frac{1}{2} - \frac{a}{w} \right) \cdot \left(\frac{w \Delta \theta}{\Delta \delta} \right) \right] \Delta \delta \right) \right] \quad (3.8)$$

where f is a parameter which is used for minimizing the portion of the reloading process during crack growth. Using the approximate estimate of δ_n based on the far-field displacement, $CTOA_n$, which is the finite element representation of CTOA shown in Fig. 3.5, may not reach $CTOA(\mu)$ precisely at the end of debonding (when $F_n = 0$ according to (3.8)). Therefore, the specimen will be reloaded until the $CTOA_n$ reaches $CTOA(\mu)$. Through trial and errors, the value of f was chosen as 0.6 for fully-plastic crack growth simulation under pure extension so as to minimize the amount of stationary crack reloading required to again increase $CTOA_n$ to $CTOA(\mu)$. Typical values of the number of time increments taken for debonding and for reloading are 36 and 8 respectively .

3.4 Crack growth simulation

A CTOD criterion, which is based on the data from Hancock, et al. (1992), is implemented for crack initiation. In this work, the relative displacement from a symmetry line of the traction-free node $n-1$ adjacent to the node, n representing the crack-tip, is taken as half of the CTOD (Fig. 3.6). At each time increment, the value of the relative displacement of node $n-1$ is measured. At the beginning of the next time increment, the value of the relative displacement of node $n-1$ for the previous time increment is compared with the critical CTOD, $CTOD_c$. If the previous value of the relative displacement of node $n-1$ reaches half of $CTOD_c$, the nodal force relaxation at node n occurs in the manner of (3.8) over several time increments. When the nodal force at node n is completely removed ($F_n = 0$) after several time increments associated with the far-field displacement, the ligament length l , which is used to determine the loading ratio μ , is reduced by Δa^n (l is kept constant during reloading) and $CTOA(\mu)$ starts to be updated using the new ligament length l . At every time increment during reloading process, $CTOA(\mu)$ and $CTOA_n$ are computed. At the beginning of the next time increment, $CTOA_n$ and $CTOA(\mu)$ of the

previous time increment are compared with each other until $CTOA_n$ reaches $CTOA(\mu)$. If $CTOA_n$ reaches $CTOA(\mu)$, the nodal force ($=F_{n+1}$) at node $n+1$ is relaxed to zero in the manner of (3.8). Otherwise, the specimen would be reloaded. A box statement of this debonding algorithm is provided in Fig. 3.7.

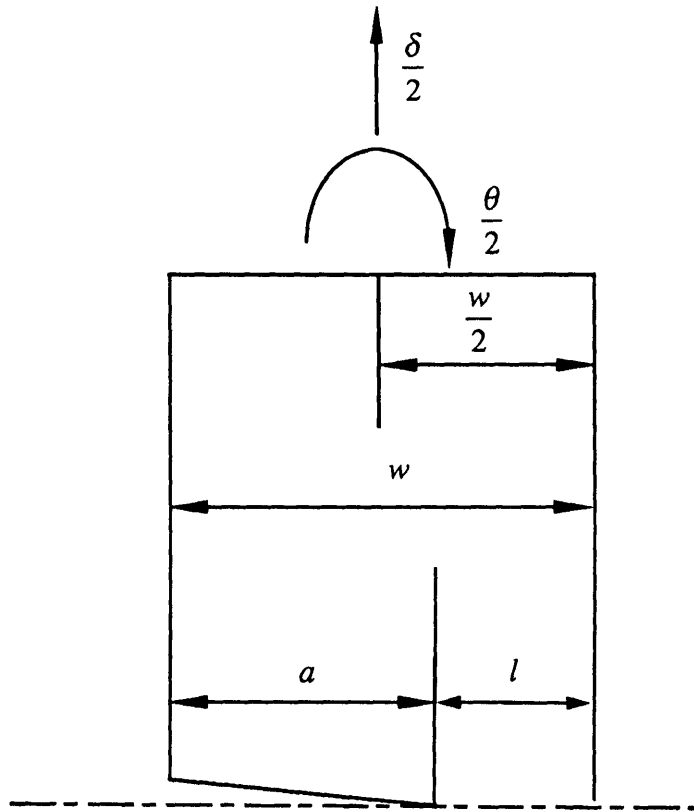


Fig. 3.1 The boundary conditions of combined displacement and rotation on a deeply-cracked single edge specimen.

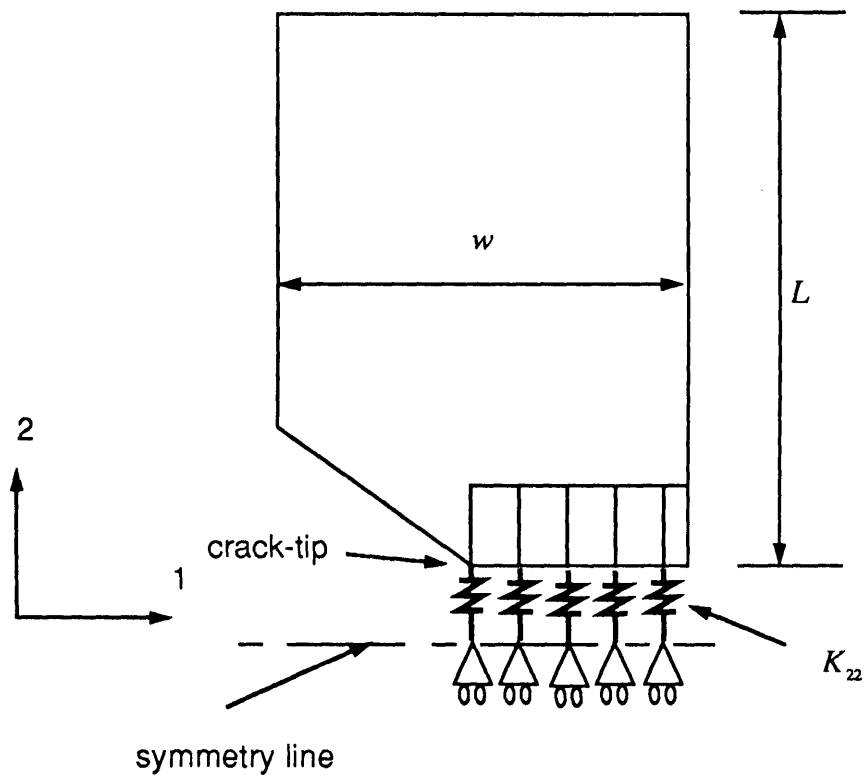


Fig. 3.2 Schematic of high stiffness spring implementation

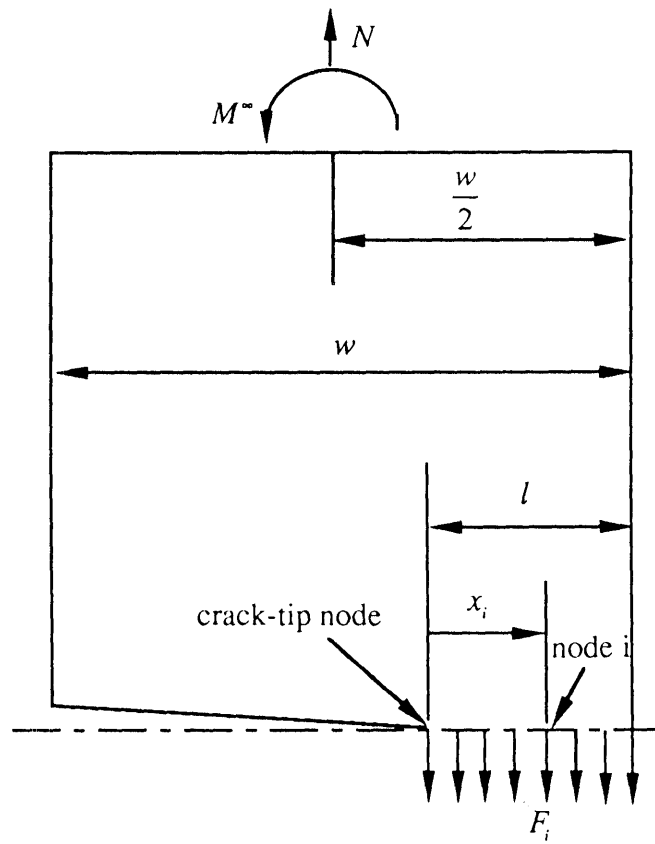


Fig. 3.3 Nodal reactions along the symmetry line.

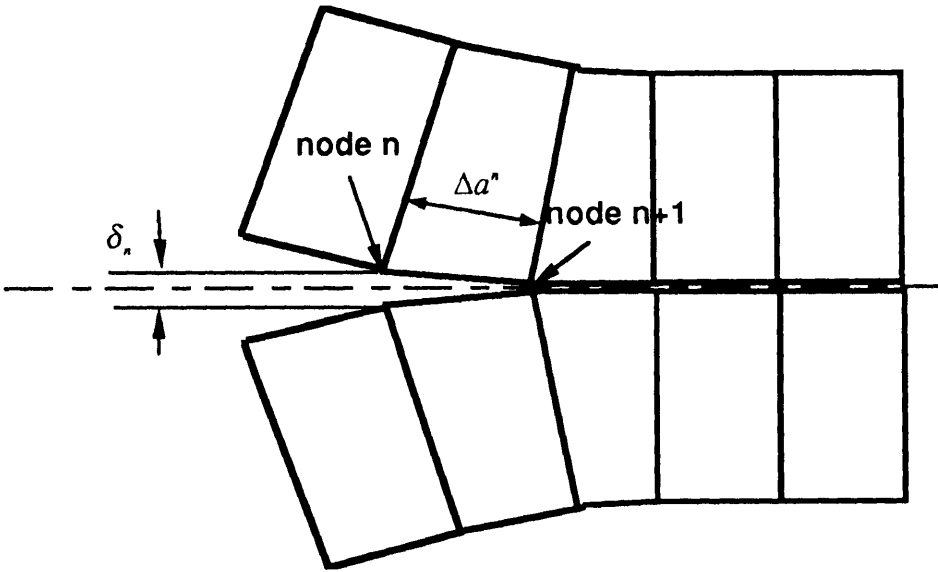


Fig. 3.4 Illustration of δ_n of the currently-releasing node n with Δa^n

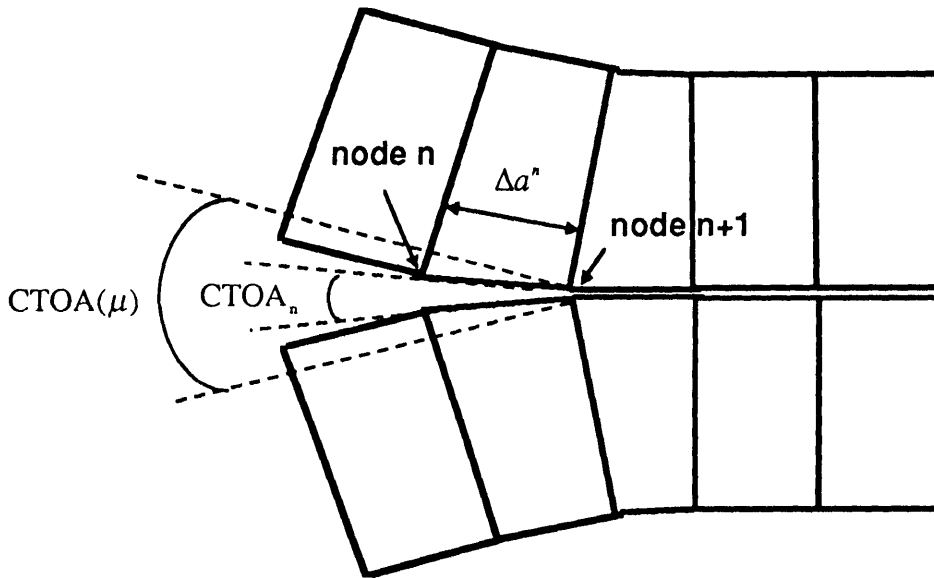


Fig. 3.5 Finite element representation of CTOA, $CTOA_n$, and the loading geometry-based CTOA, $CTOA(\mu)$

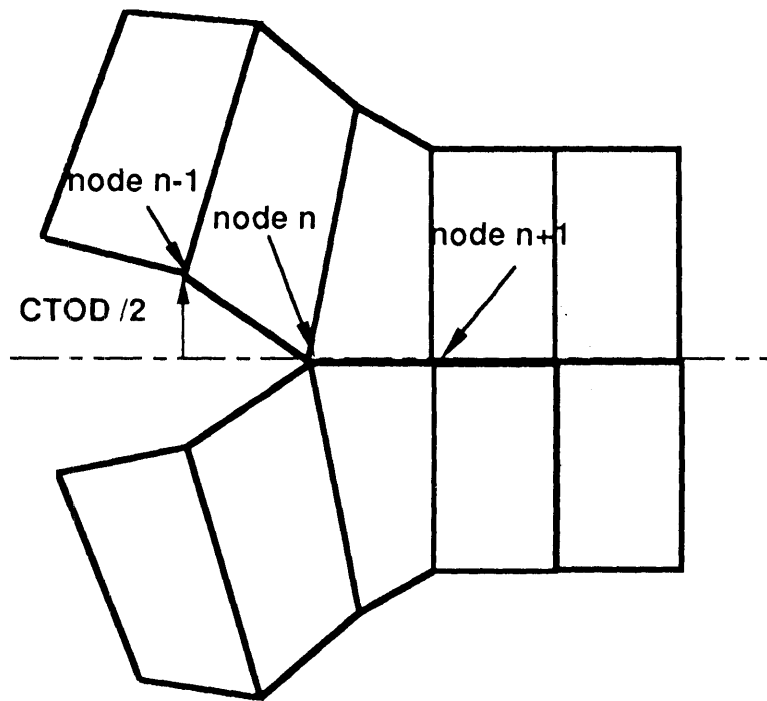
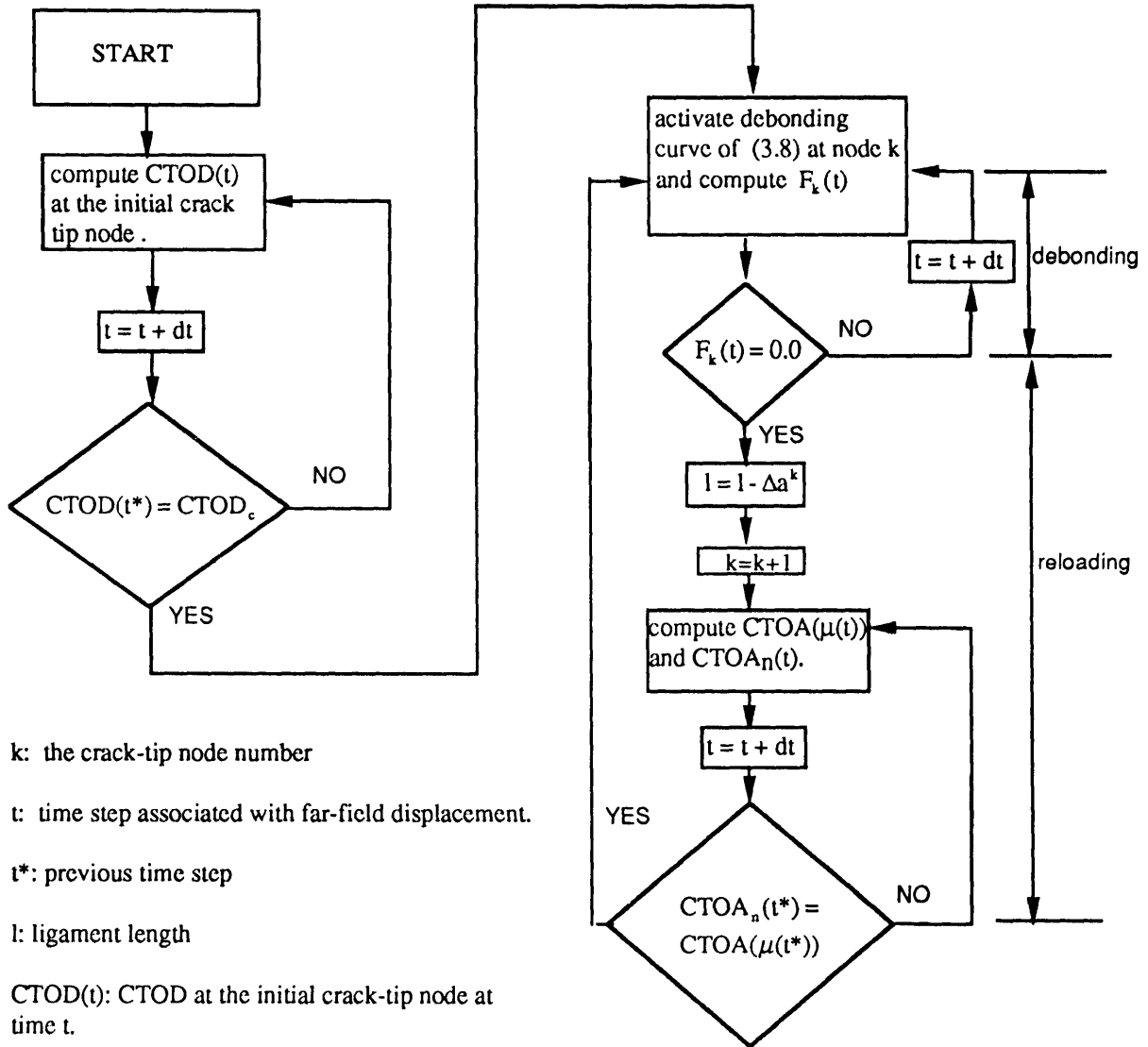


Fig. 3.6 Finite element representation of CTOD.



k : the crack-tip node number

t : time step associated with far-field displacement.

t^* : previous time step

l : ligament length

$CTOD(t)$: CTOD at the initial crack-tip node at time t .

$CTOD_c$: critical CTOD at crack initiation

Δa^k : element size directly ahead of the crack-tip node

$F_k(t)$ traction at node k and time t .

$CTOA_n(t)$: $CTOA_n$ at time t . (illustrated in Fig. 3.5)

$\mu(t)$: loading ratio at time t

$CTOA(\mu(t))$: loading geometry-based CTOA at time t .

Fig. 3.7 Numerical algorithm of crack growth simulation

Chapter 4

Results and Discussion

4.1 Method

A plane strain single edge cracked specimen composed of an isotropic elastic/perfectly-plastic material is modeled using with 4-node plane strain elements. Using symmetry arguments, only half of a specimen is considered (Fig. 4.1). All the crack growth simulations reported in this thesis are carried out under pure extension ($N > 0$, $\theta^{loc} = 0$; θ^{loc} is the rotation at the far-field loading point). The relative initial crack depth a_0/w and the relative length of the specimen, L_0/w , are 0.5 and 3.0, respectively. The nodes on the symmetry line of the specimen are modified in order to be released upon the satisfaction of the chosen fracture criterion (CTOD or CTOA). Upon satisfaction of the fracture criterion, the force at the node representing the crack tip is relaxed to zero, and the crack advances by one element length.

Two different types of mesh configurations are developed for simulating crack growth under pure extension. Most of the present results have been computed using Mesh B (Fig. 4.3), but some results obtained using Mesh A (Fig. 4.2) will also be presented to illustrate the sensitivity of the predictions to the choice of mesh configuration.

Mesh A

A focused mesh configuration is not used for our crack growth simulations. Instead, a mesh aligned with the expected flow field (Kim, et al, 1994a) for a pure extension loading condition and non-hardening material is developed to approximate the deformation field as closely as possible (Fig. 4.2). In order to maintain the same scale as crack grows, the mesh ahead of the crack-tip is regraded so that the ratio of the element length directly in front of the crack-tip, Δel , to the current length of the ligament, l , is nearly constant: $\Delta el/l \approx 0.035$

Mesh B

Mesh B is highly refined in the region of the first quarter of the initial ligament (Fig. 4.3). For these elements, the ratio of the element length directly ahead of the crack-tip in the refined zone Δel to the original ligament l_0 is given as 3×10^{-3} . However, limitations on computing allow for the refined mesh to be applied on only 30% of the original ligament. Mesh orientation is generated in the same manner as that of Mesh A.

4.2 Comparison with the line-spring model (Lee and Parks, 1994)

The line-spring model of Lee and Parks (1994) can be used only under small geometry changes. So, in order to compare the results of the present FEM/continuum model with those of the line-spring model, small geometry change analyses are conducted on both Mesh A and Mesh B. Material constants such as tensile yield strain, ϵ_y , and yield strength in shear, τ_y , are 2.27×10^{-3} and 271 MPa respectively. The critical relative CTOD at crack initiation, δ_c/l_0 , is given as 0.02. The hole nucleation parameter $B(\sigma_c)$ is assumed to be zero, and the critical hole growth ratio parameter A is set to be 0.5.

Fig. 4.4 shows the normalized axial force, $N/(2\tau_0 l_0)$, vs. total loading point displacement, δ^{tot}/l_0 , under pure extension. The total loading point displacement δ^{tot} is given as the sum of the loading point displacements of both halves of the specimen as shown in Fig 4.1. The cross symbol on the plot indicates crack initiation. In Fig. 4.4, the sensitivity of the predictions to the choice of the mesh configuration between Mesh A and Mesh B is clearly illustrated. Also, the results obtained using Mesh B are observed to be in excellent agreement with those of the line-spring model. Such an agreement between the two models verifies the consistency of the formulations, which is implemented in the line-spring model under pure extension and the assumption of small geometry change.

Also, based on such an excellent agreement, Mesh B is chosen for further investigation of crack extension behavior, which is given in the next following section, under both small and large geometry changes.

4.3 Crack growth simulations under pure extension

Fully plastic crack growth in a pre-cracked specimen consists of initial, transient and steady growth. Since our concern is focused on the crack tip field of quasi-steady crack growth, the crack growth simulation should be made such that the crack growth reaches the steady state in the region of the refined mesh (Mesh B). But, due to the limitation of the computing time as mentioned before, the range of the refined mesh can not be fully extended. Instead, the yield strain (elastic strain) is reduced in order to compress the transient region. Based on the results from Kim, et al. (1994c), it can be observed that by reducing the yield strain of the material, crack growth can reach the steady state more quickly (i.e. with less imposed displacement). The tensile yield strain is given as 0.001, and other material properties are given as specified in the previous section. Here, both

small geometry change (SGC) and large geometry change (LGC) analyses under pure extension are carried out.

Load-deflection curve

Fig. 4.5 (a) shows the normalized axial force $N/(2\tau_0 l_0)$, vs. normalized total loading point displacement δ^{tot}/l_0 . The axial force decreases almost linearly with increasing loading point displacement immediately after crack initiation (marked by a cross symbol). Also, the effect of the critical hole growth ratio parameter A on crack extension behavior can be observed: increasing the value of A slows down the crack growth rate. Fig. 4.5 (c) shows the axial force, which is normalized by the product of the yield strength in shear τ_y and current ligament length l , vs. total loading point displacement δ^{tot}/l_0 ; l is taken as the value, which was defined in the debonding algorithm shown in Fig. 3.7. Here, this curve for SGC indicates that the load state during crack growth remains on the yield locus which Rice (1972) and Kim, et al. (1994b) proposed for deep single edge specimen ($N/2\tau_y l=1$ for pure extension). However, $N/2\tau_y l$ in LGC is observed to be slightly greater than unity as shown in Fig. 4.5 (c). The discrepancy observed in LGC implies that the stresses along the ligament are not constant, but some stress elevation near the crack-tip is expected.

CTOA

Evolution of CTOA with the change of deformation is shown in Fig. 4.5 (d) as the crack grows. A slight difference between LGC analysis and SGC analysis can be observed. As the crack grows, the CTOA in the SGC increases to the maximum permitted value of CTOA for $\mu=0$, while the CTOA in LGC saturates at some point, or even decreases slowly. Since the current algorithm for crack growth determines the CTOA from the load ratio parameter μ for the case of LGC, some stress elevation near the crack tip,

which may induce some bending moment in the net section and eventually reduce the loading geometry-based CTOA, can be expected to be present in the LGC solution.

Crack tip triaxiality

Due to the finite element discretization and the particular nodal release technique employed to simulate crack growth, there is an ambiguity, to within one finite element, in the exact position of the crack-tip as sensed by the numerical solution. However, using a simple geometric argument (McClintock, 1994), the current crack-tip position can be extrapolated from the displacement of the node which is currently being released, as shown in Fig 4.6. The position obtained from the technique is adopted here as instantaneous crack-tip, which is taken as the origin for the following stress and strain distributions of the crack-tip field.

Fig. 4.7 shows the distribution of normalized mean normal stress, σ_m / τ_y , ahead of the crack-tip at the relative crack extension $(a - a_o) / l_o = 0.16$. Here, $\sigma_m = \frac{1}{3} \sum_i \sigma_{ii}$. In Fig. 4.5 (a) through (d), the data points corresponding to $(a - a_o) / l_o = 0.16$, are indicated by a open circle. One interesting point in both Fig. 4.7 (a) and (b) is that the value of σ_m / τ_y in LGC is higher than in SGC by 13% for $A=0.5$ and by 30% for $A=1.0$ at the radius $r = 1.7 \times 10^{-2} l$ from the crack-tip, while for the fully plastic stationary crack under pure extension, the theoretical value of σ_m / τ_y ahead of the crack-tip is unity (Lee and Parks, 1993). However, a deformation field consisting of one single slip line, which Kim, et al. (1994c) proposed in their line-spring model as the deformation field of growing crack under pure extension in a non-hardening material, does not account for such elevation of the crack-tip triaxiality observed in LGC.

It can be argued that the relatively high stress triaxiality (the normalized mean normal stress, σ_m / τ_y) at the crack tip in LGC results indirectly from the change in the back face angle ω where the shear band intersects the back surface of the specimen (defined in

Fig. 4.8). As the crack grows, the back surface of the specimen cannot be maintained as flat, as it was initially. Therefore, the increase of the back face angle permits a distortion of the single slip line field which is found under pure extension under the assumption of small geometry change. Instead, a slip line field with the centered fan as shown in Fig 4.8 develops. In the present numerical results under LGC, the ratio of the ligament length l to the distance h (the perpendicular distance from the symmetry line to point b in Fig. 4.8), is found to be greater than unity, while this ratio is unity for those simulations performed in SGC. By considering the slip-line field with a centered fan, the stress triaxiality on the symmetry plane starts to increase at the point $a1$, where two 45° slip lines intercept each other and $\sigma_m / \tau_y = 1$, and the maximum stress triaxiality occurs at the crack-tip (Detailed computation for the stress triaxiality in the slip line field based on the ratio h/l is given in Appendix 4.1). The predictions of the state of the stress triaxiality ahead of the crack-tip using the theory of the slip-line field is found to be generally in good agreement with the present numerical results, as shown in Fig. 4.7.

The comparison between Fig. 4.7 (a) and (b) illustrates the (indirect) effect of the critical hole growth ratio parameter A on the stress triaxiality at the crack-tip in LGC. This comparison also supports the previous argument for the slip-line field with the centered fan as shown in Fig. 4.8: raising the loading geometry-based CTOA using a higher value of A , the rigid/plastic behavior of the specimen in the fully plastic regime causes an increased back face angle ω . Consequently, the increase of the back face angle increases the permissible range of the angle of the centered fan ϕ . The maximum permissible span of the fan is $\phi = 2\omega$ based on the theory of slip line fields. Larger values of ϕ lead to center-line triaxiality increase over larger fraction of the ligament. Therefore, following the theory of slip-line fields given in Appendix 4.1, higher stress triaxiality is obtained at the crack-tip for the higher value of A , as illustrated in Fig 4.7. Hydrostatic stress contours in LGC solutions shown in Fig. 4.10 lend added credence to the existence of the newly proposed slip line field on the ligament under pure extension. Following the contour line of

$\sigma_m / \tau_y = 1.1$, some perturbation of the hydrostatic stress variation ahead of crack-tip is observed where the element size starts to increase. Such a perturbation results from the change of element size.

Plastic strain near the crack-tip

Fig. 4.11 shows the normalized incremental equivalent plastic strain $\Delta \bar{\epsilon}^p$ contours at $(a - a_0) / l_0 = 0.16$ obtained from LGC analyses. Here, the normalized far-field displacement $(\delta^{tot} / 2) / l_0$ corresponding to $\Delta \bar{\epsilon}^p$ is 0.01. The active plastic deformation area indicated by the variation of contours matches our expected slip line field. Near the crack-tip the shear band is directed at 45° from the symmetry line. Further away from the crack-tip, the shear band gets more diffused, but toward the back surface, the shear band becomes relocalized due to the change of the back face angle. The Mises stress σ_e (normalized by tensile yield strength σ_y) contours shown in Fig. 4.12 indicate that the active plastic zone corresponding to the slip line field is inside the region where the von Mises yielding criterion is satisfied.

We also obtained values of incremental plastic strain extrapolated from the averaged nodal values to the points on the circle of the chosen radius. The incremental equivalent plastic strain $\Delta \bar{\epsilon}^p$ vs. θ is shown at the radius $r = 5.0 \times 10^{-2} l$ (Fig. 4.13 (a) and Fig. 4.14 (a)) from the crack tip, and at the radius $r = 1.7 \times 10^{-2} l$ (Fig. 4.13 (b) and Fig. 4.14 (b)) respectively. In SGC the angle of the shear band from the symmetry line is 45° , which coincides with the theoretical value of the slip-line angle of the stationary single edge crack under pure extension. The angle of the shear band in LGC is observed to vary depending on the chosen radius from the crack-tip, as expected from the incremental equivalent plastic strain contours. Fig. 4.15 demonstrates that the total plastic strain diffuses ahead of the crack-tip. Such diffusion of plastic strains smoothes the plastic strain discontinuity across the shear band to some extent.

Backface angle

Backface angles at three different crack depths are shown in Fig. 4.16. As crack grows, the back face angle ω is observed to increase, but seems to saturate rapidly (Fig. 4.17). Such tendency indicates that as crack grows further, the crack-tip field, which is observed to be affected by the change of back face angle, may converge to steady state.

Summary of results and Discussion

Table 1: Characterization Parameters

	A=0.5		A=1.0	
	SGC	LGC	SGC	LGC
CTOA(μ) (deg)	29.6	29.2	72	68.52
ω (deg)	11.9	8.53	17.2	13.69
l/h	1	1.13	1	1.26
θ_s (deg)	45	45	45	41.53
σ_m/τ_y	1.16	1.31	1.11	1.61
$\gamma_r(=\sqrt{3}\bar{\epsilon}^r)$	0.44	0.44	1.00	1.00

Table 1 presents the values of parameters characterizing the deformation field for two different values of the ductility parameter A at the relative crack extension $(a - a_0)/l_0 = 0.16$. Here, θ_s is denoted as the slip line angle and the value is taken as the angle of the shear band from the symmetry line at the radius $r = 1.7 \times 10^{-2} l$ and the value of the crack-tip triaxiality σ_m/τ_y is also taken at $r = 1.7 \times 10^{-2} l$. Using the slip-line field based on the ratio l/h , estimates for the crack-tip triaxialities corresponding to $A=0.5$ and $A=1.0$ are 1.26 and 1.47 respectively. Due to the finite element discretization procedure, the shear band obtained based on SGC analyses is found to be slightly diffused, crossing two rows of the elements. Due to such diffusion of the shear band, the crack-tip triaxiality even in SGC is observed to be slightly higher than the theoretical value ($=1$) of the crack-tip triaxiality for crack growth under pure extension.

By observing the values of the stress triaxiality at the crack-tip based on LGC analyses, the inconsistency of the crack growth model using the loading geometry-based CTOA as a fracture criterion in a non-hardening material, can be clearly addressed. For $A=1.0$ the fracture (shear) strain, γ_f , corresponding to the present value of crack-tip triaxiality in LGC obtained through (2.6) is found to be about only half of the fracture strain presented in Table 1. Assuming a partial Prandtl field at the crack-tip, the stress triaxiality on the shear band, σ_s/τ_s , which is adopted as the crack-tip triaxiality in (2.6), can be approximated simply from the stress triaxiality on the symmetry line directly ahead of the crack-tip, σ_m/τ_m (Lee and Parks, 1993). Furthermore, invoking (2.5), the estimated value of CTOA for $A=1.0$ based on the present value of the crack-tip triaxiality in LGC is also only about 40% of the present value of the loading geometry-based CTOA(μ) under pure extension. Therefore, the value of the CTOA imposed based on loading configuration in the present crack growth model is overestimated. The major discrepancy is that for LGC, σ_s no longer depends on the load ratio μ in the way derived by Kim, et al. (1994a) and numerically verified by Lee and Parks (1993). Considering the geometry change effect of the back surface on the crack-tip field, as the back face angle becomes large enough to build up high stress triaxiality at the crack-tip during crack growth, CTOA would tend to decrease instead of saturating at the maximum value corresponding to $\mu = 0$. In fact, such tendencies are indirectly observed in Fig. 4.5 (d), corresponding to $A=1.0$, due to the drift of μ away from zero caused by the build-up of higher crack-tip stress levels. This feature of CTOA variation shows that the deformation-induced geometry change induces bending moment on the remaining ligament, but it does not account for the direct effects of the geometry change on the crack-tip field and hence on local fracture strain.

APPENDIX 4.1

With the slip line field as shown in Fig 4.8, the steps to determine the normal stress σ_m are the following:

Step 1) Choose the point $a1$, where the mean normal stress σ_m is simply equal to the shear strength τ_y .

Step 2) Following from point $a1$ to point $a1'$ and using the Hencky equation of equilibrium, the mean normal stress σ_m is built up as

$$\sigma_m = 2\tau_y(\alpha) + \tau_y. \quad (1)$$

Step 3) In the same manner as in step 2, the mean normal stress σ_m at point $a1''$, which is on the symmetry line, is determined as

$$\sigma_m = 2\tau_y(\alpha + \beta) + \tau_y. \quad (2)$$

However, on the symmetry line, $\alpha = \beta$. The mean normal stress is rewritten as

$$\sigma_m = 2\tau_y(2\alpha) + \tau_y. \quad (3)$$

Step 4) Using the tabulated data from Chakrabarty (1987), the relative distance d/h on the symmetry line is plotted against α , as shown in Fig. 4.9 (a).

Step 5) Following the symmetry line, x_1/l is determined corresponding to $\alpha (= \beta)$ for $A = 0.5$ and $A = 1.0$ respectively based on the relationship shown in Fig. 4.9 (a) (Fig. 4.9 (b)).

Step 6) σ_m / τ , is determined in terms of x_1/l using (3) and the relationship shown in Fig. 4.9 (b) (Fig 4.9 (c)).

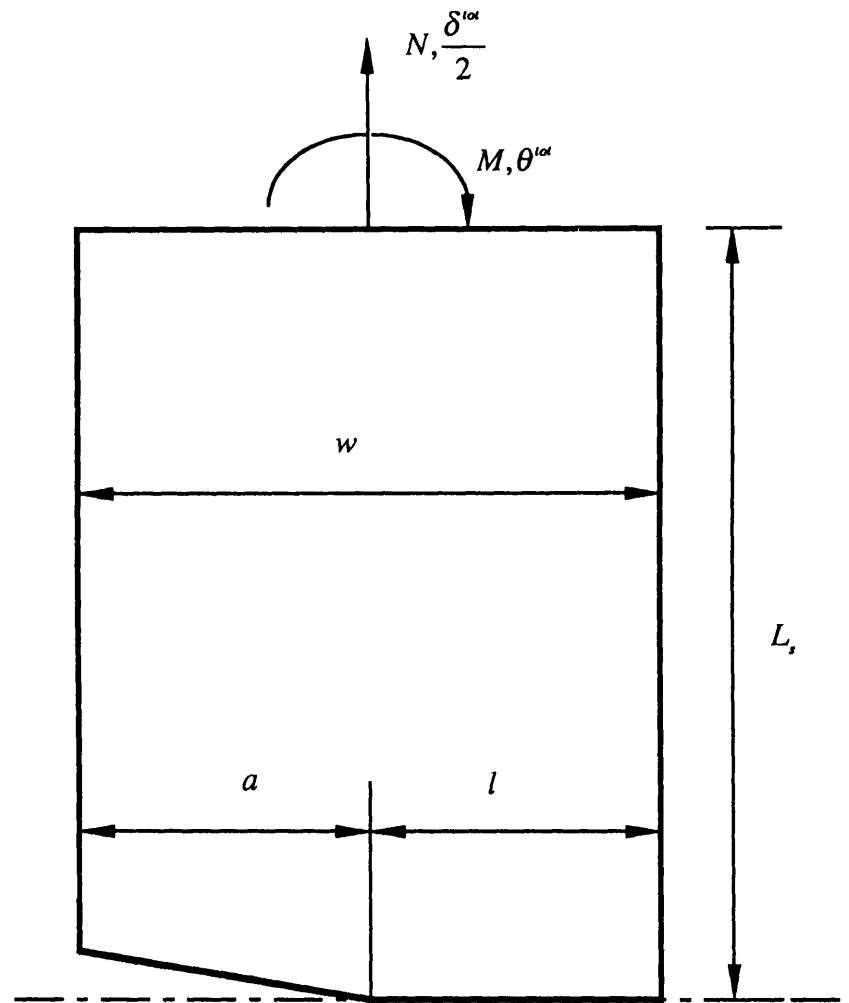
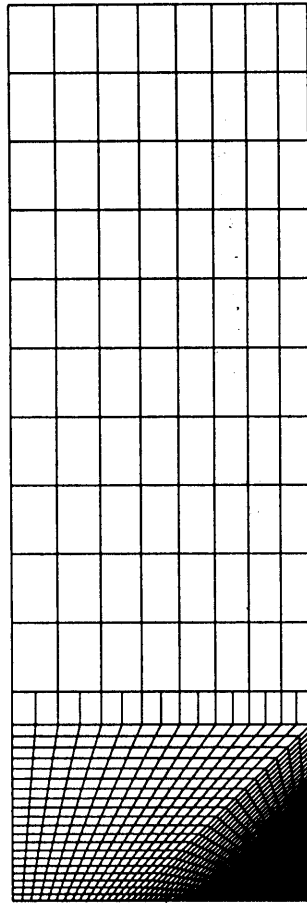
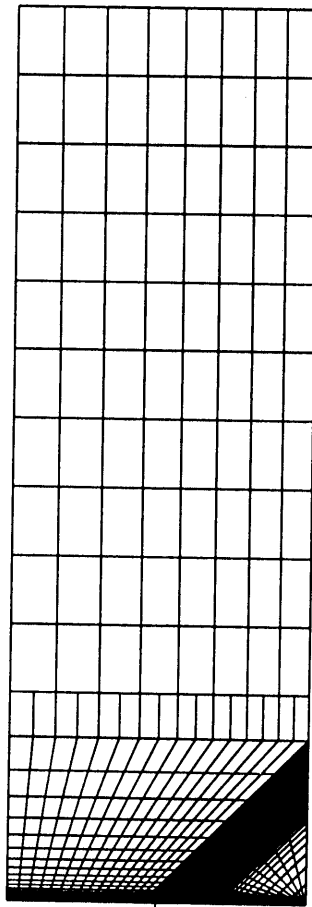


Fig. 4.1 A deeply-cracked single edge specimen subject to combined tension and bending.



↑
initial crack-tip

Fig. 4.2 Mesh A



↑
initial crack-tip

Fig. 4.3 (a) Mesh B

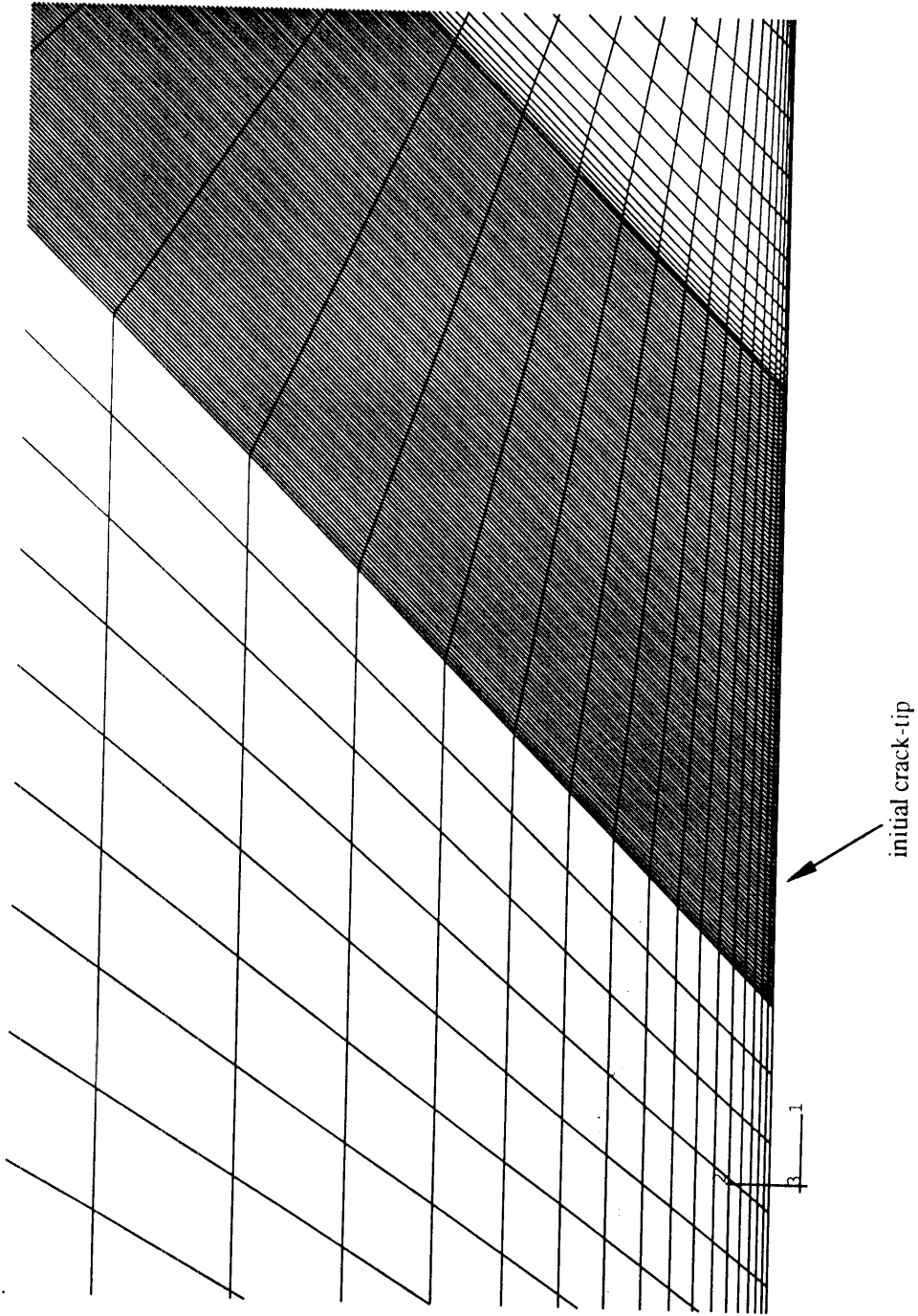


Fig. 4.3 (b) Arrangement of elements near the initial crack tip in Mesh B

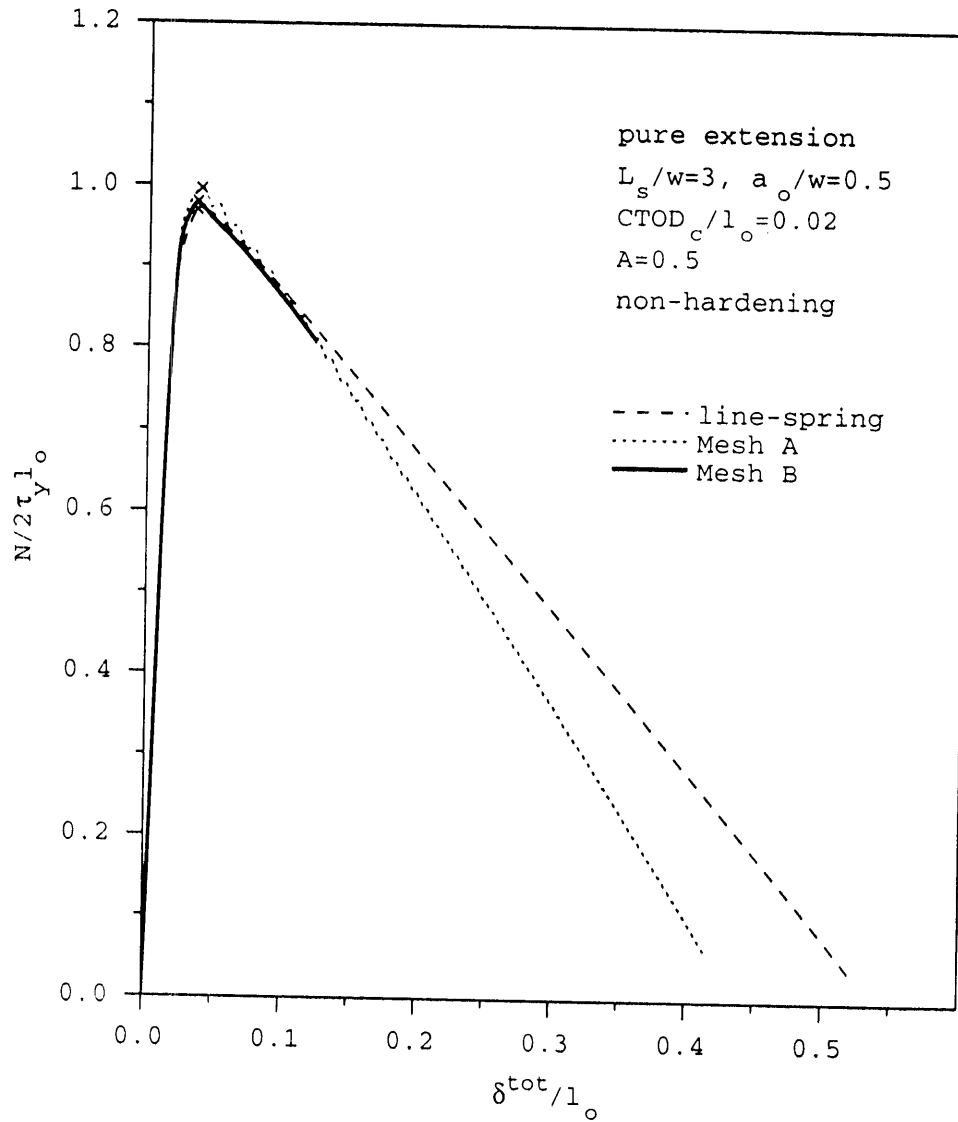


Fig. 4.4 (a) Normalized axial force $N/(2\tau_y l_o)$ vs. total loading point displacement δ^{tot}/l_o of the plane strain single edge specimen with initial crack depth $a_o/w = 0.5$ under pure extension ($N > 0, \theta^\infty = 0$) for $A = 0.5$ with $B(\sigma_y) = 0$

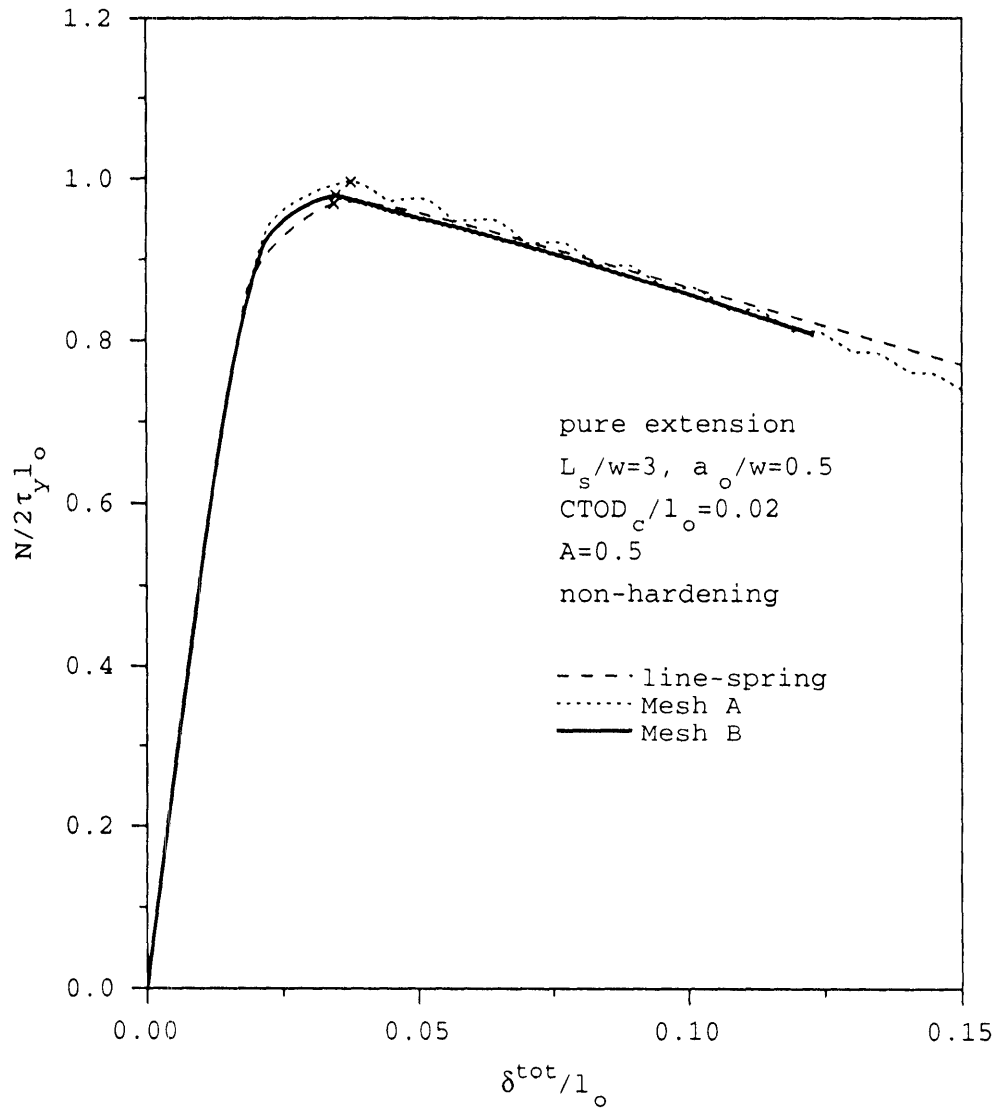


Fig. 4.4 (b) Expanded scale of $N/(2\tau_y l_o)$ vs. δ^{tot}/l_o for the early part of crack growth.

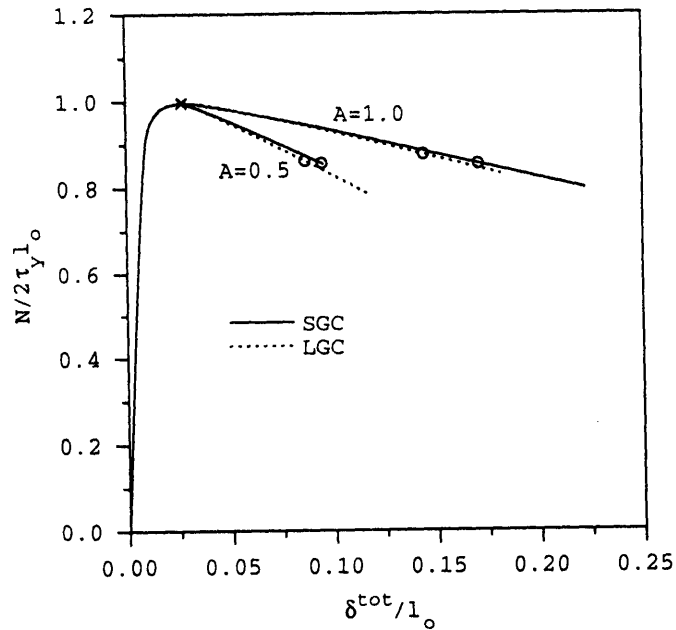


Fig. 4.5 (a) Normalized axial force $N/(2\tau_y l_0)$ vs. total loading point displacement δ^{tot}/l_0 of the plane strain single edge specimen with initial crack depth $a_0/w = 0.5$ under pure extension ($N > 0$, $\theta^{\text{tot}} = 0$) for $A = 0.5, 1.0$ with $B(\sigma_x) = 0$.

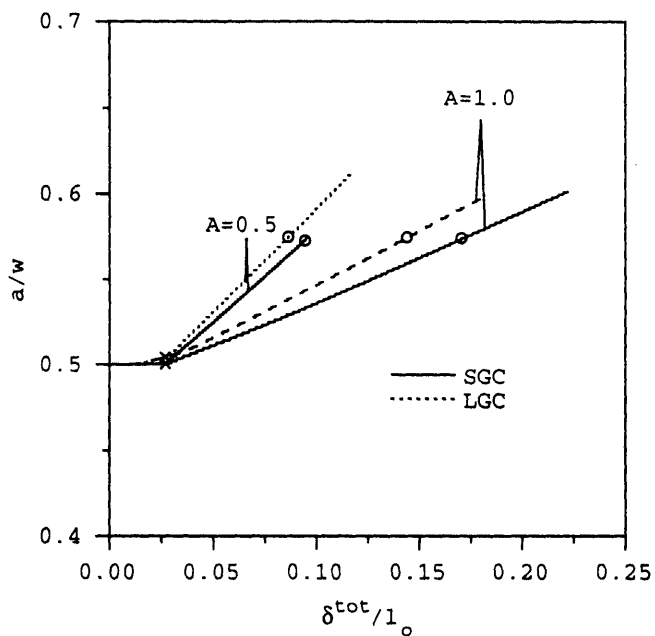


Fig. 4.5 (b) Normalized crack depth a/w vs. total loading point displacement δ^{tot}/l_0 .

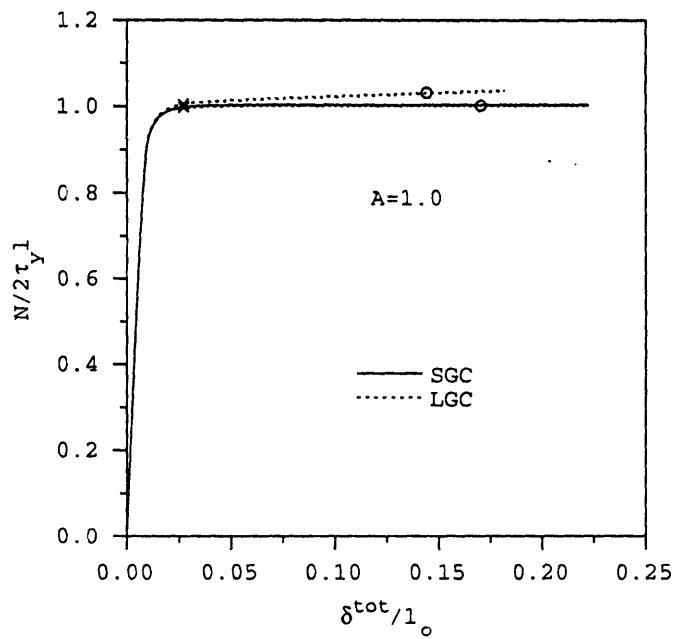
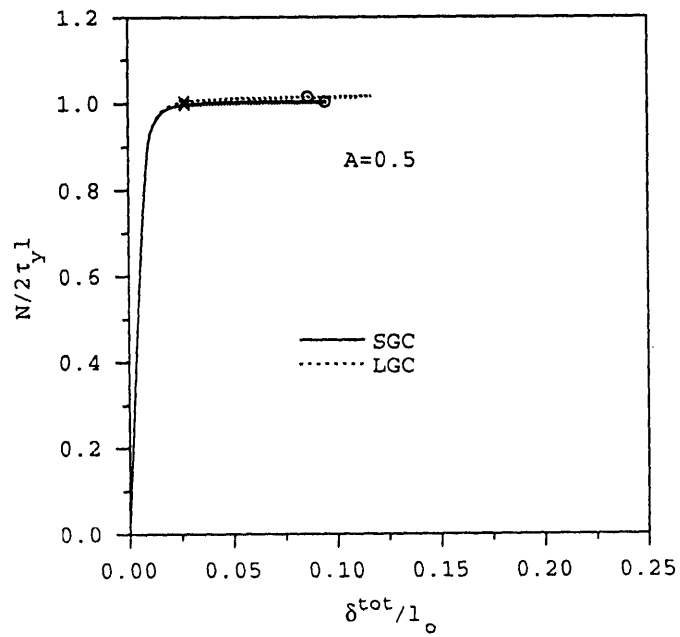


Fig. 4.5 (c) Normalized axial force $N/(2\tau_y l)$ vs. total loading point displacement δ^{tot}/l_0 for $A=0.5$ (top) and $A=1.0$ (bottom).

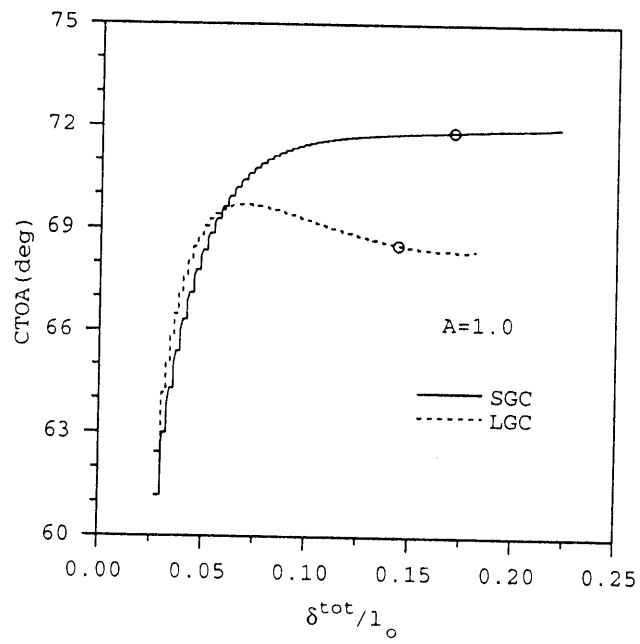
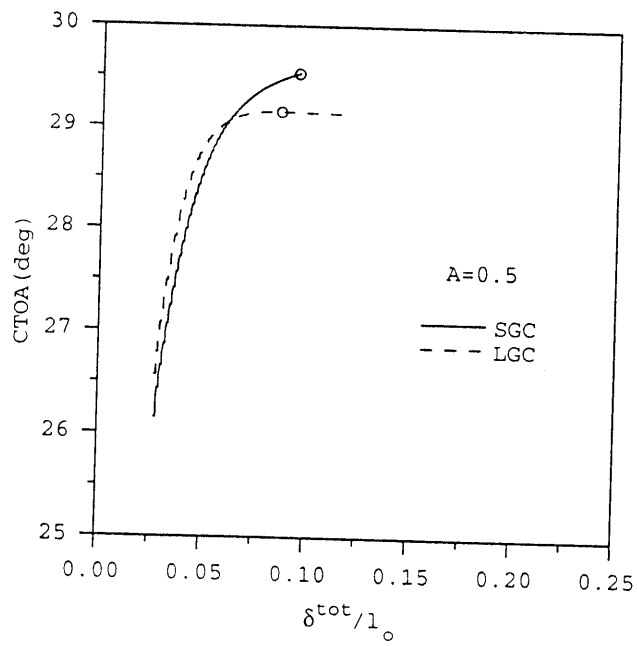


Fig. 4.5 (d) CTOA(μ) vs. total loading point displacement δ^{tot}/l_0 after crack initiation for $A = 0.5$ (top) and $A = 1.0$ (bottom).

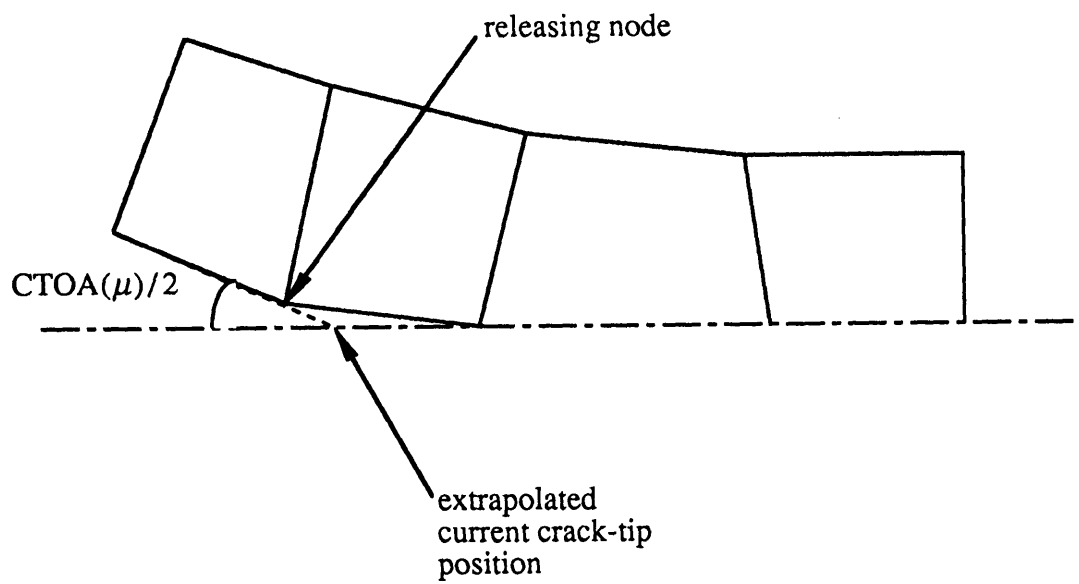


Fig. 4.6 Finite element representation of the current crack-tip position.

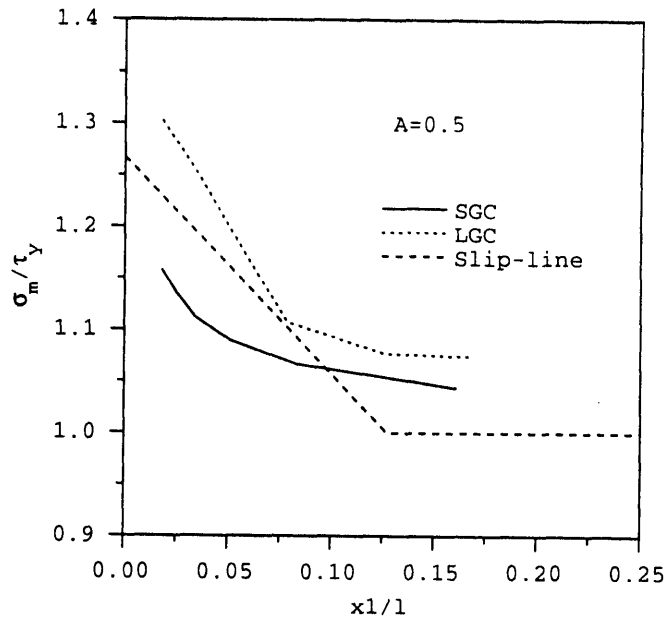


Fig. 4.7 (a) Stress triaxiality σ_m/τ_y , vs. x_1/l for $A=0.5$.

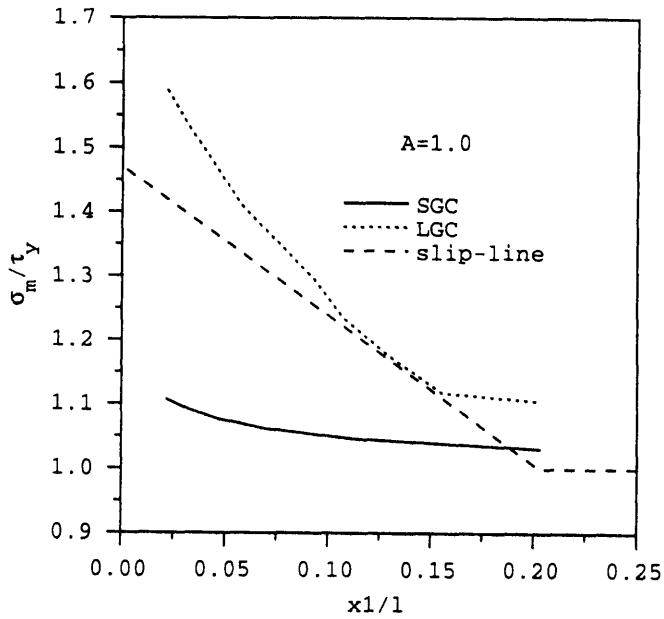


Fig. 4.7 (b) Stress triaxiality σ_m/τ_y , vs. x_1/l for $A=1.0$.

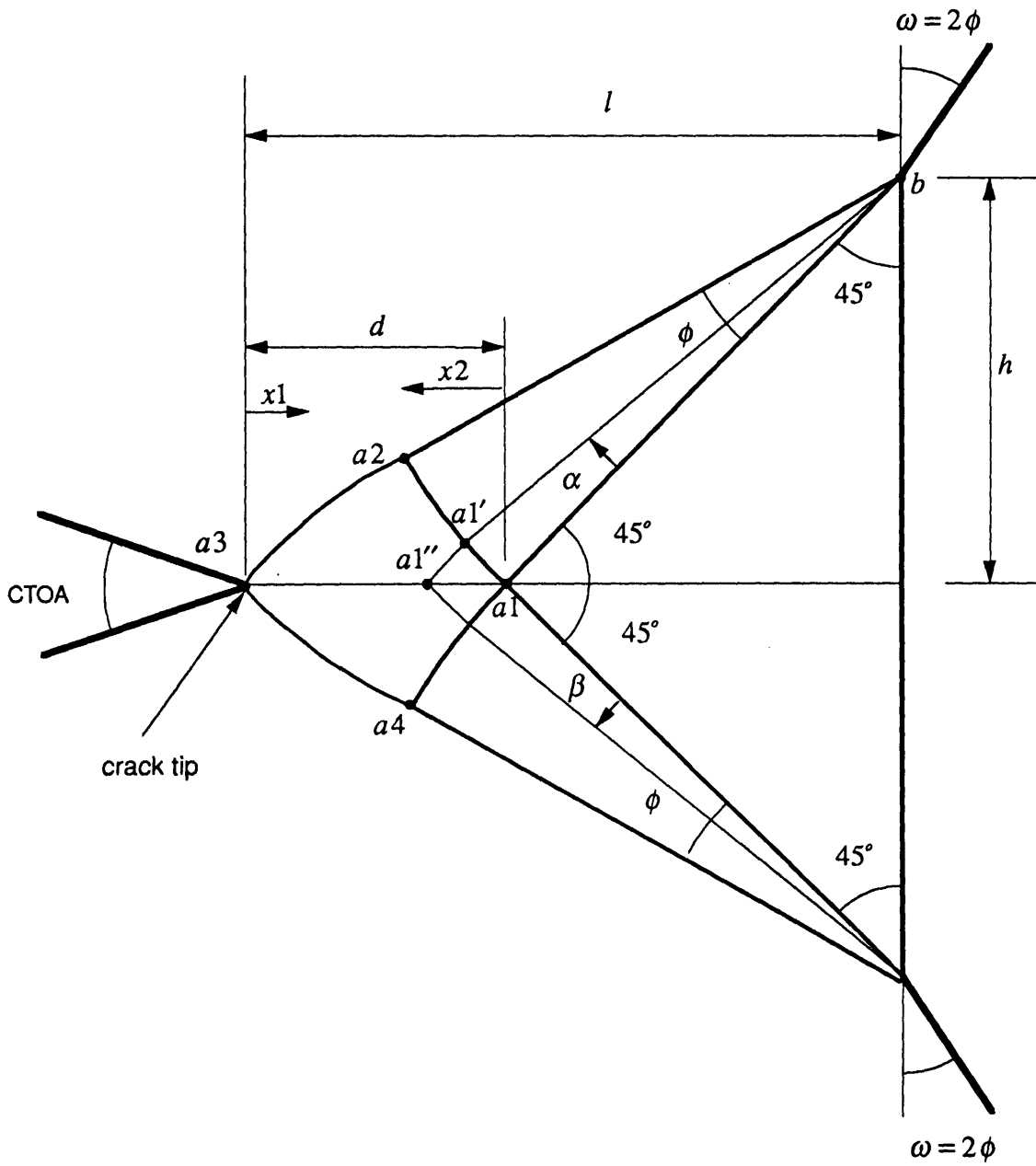


Fig. 4.8 Slip-line field on a deeply-cracked single edge specimen under pure extension. Back face angle ω is also shown.

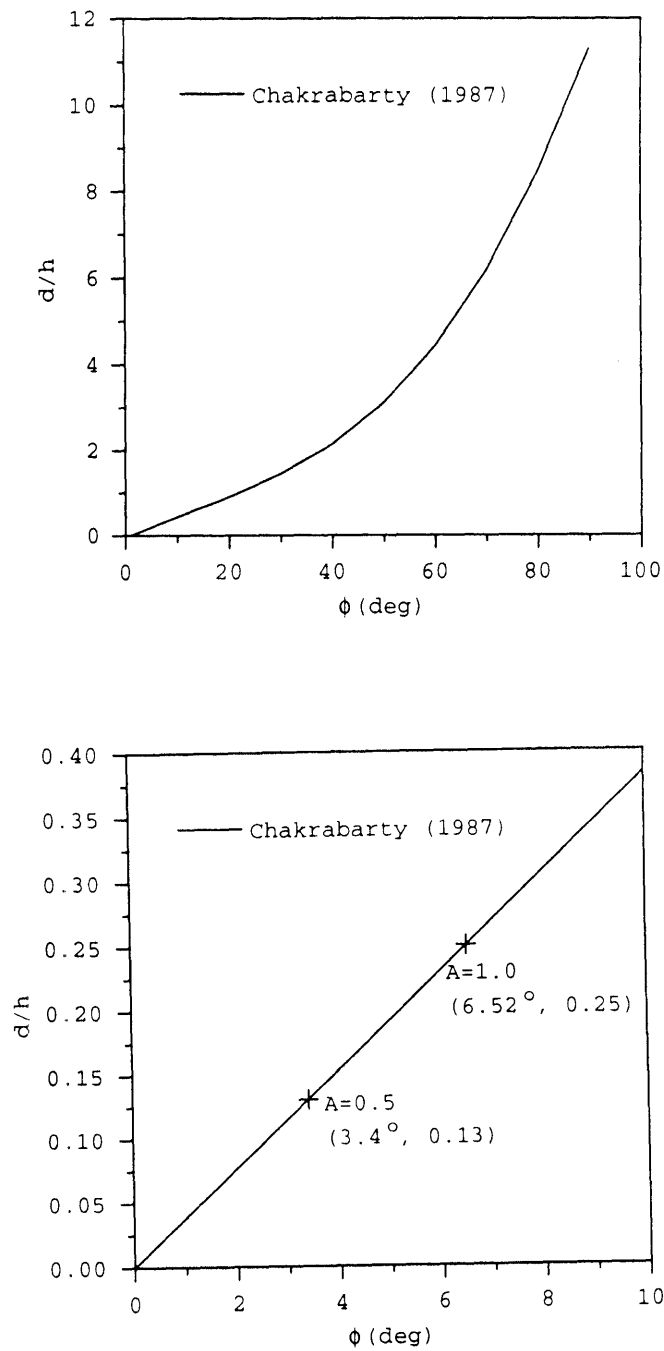


Fig. 4.9 (a) d/h vs. the angle of the centered fan of the slip-line field ϕ (top).
 For $\phi < 10^\circ$ the values ϕ for $A = 0.5$ ($d/h = 0.13$) and $A = 1.0$ ($d/h = 0.25$) are shown (bottom).

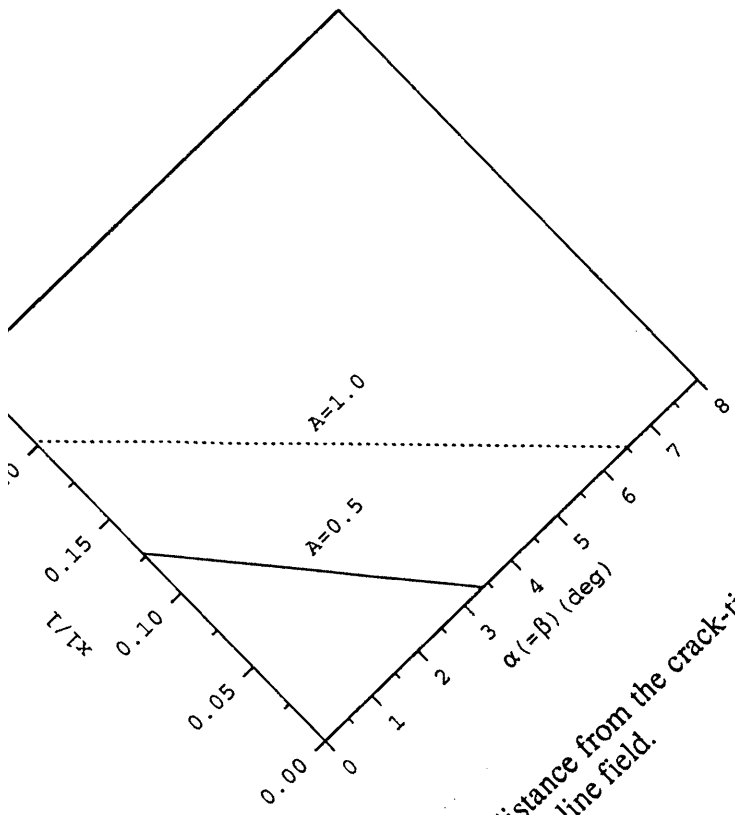


Fig. 4.9 (b) Predictions of distance from the crack-tip x_1/l vs. $\alpha (= \beta)$ for $A=0.5, 1.0$ based on the slip-line field.

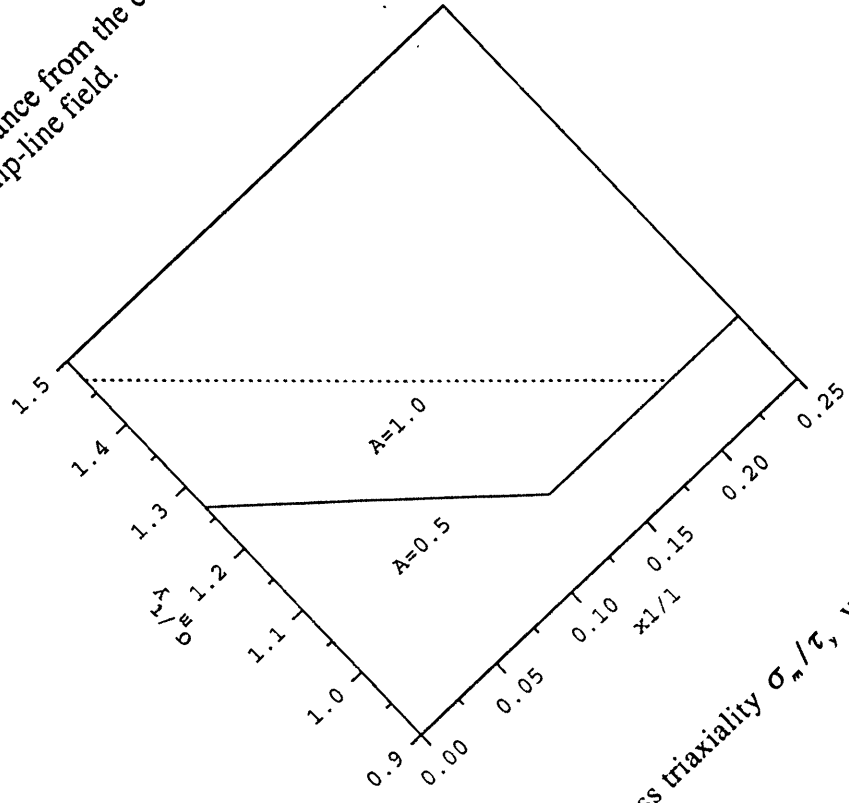


Fig. 4.9 (c) Predictions of stress triaxiality σ_m/σ , vs. x_1/l for $A=0.5, 1$ on the slip-line field.

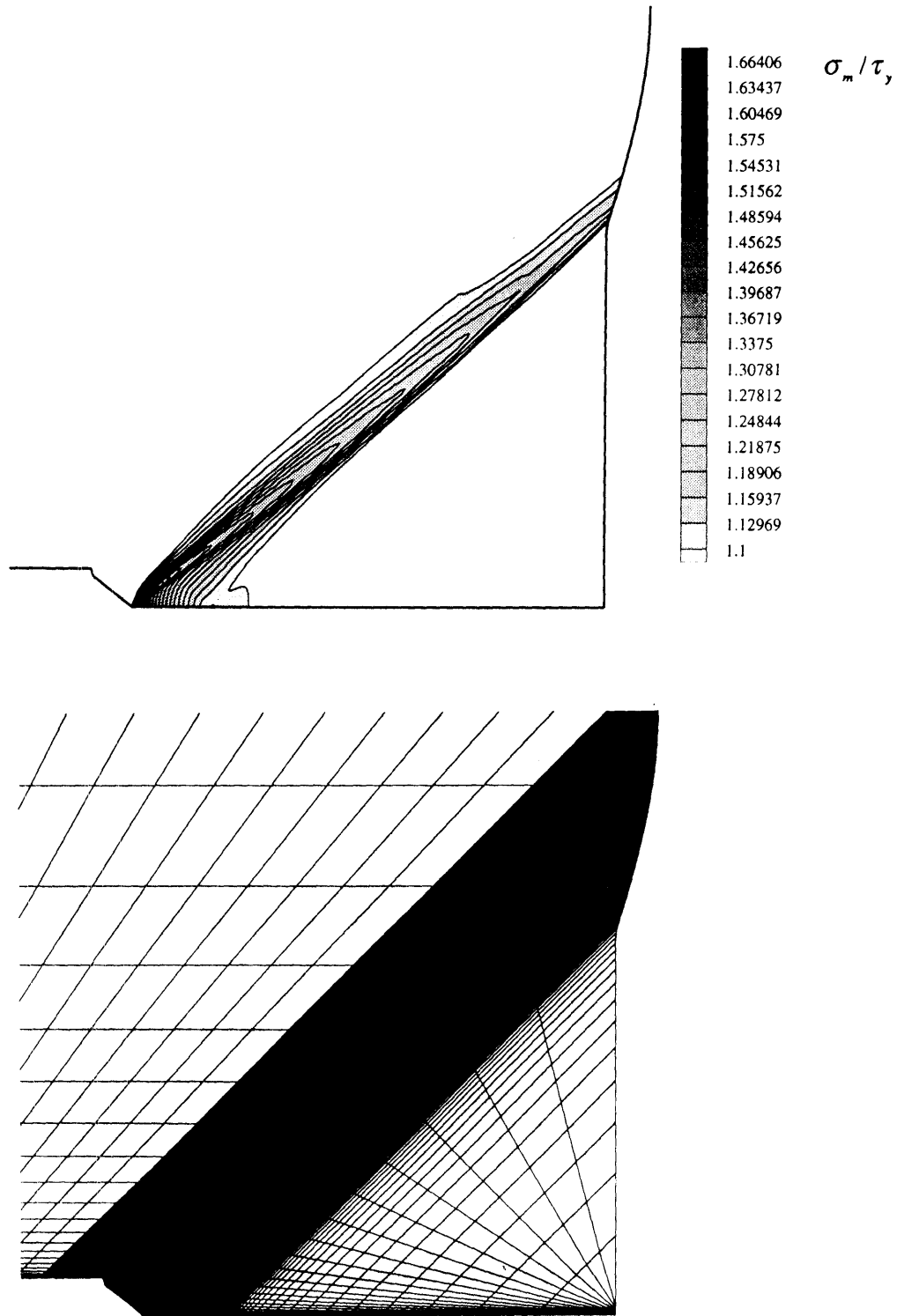


Fig. 4.10 (a) Stress triaxiality σ_m / τ_y contours for $A = 1.0$ and $(a - a_0) / l_0 = 0.16$ (top).
 Finite element mesh corresponding to the region of σ_m / τ_y contours (bottom).

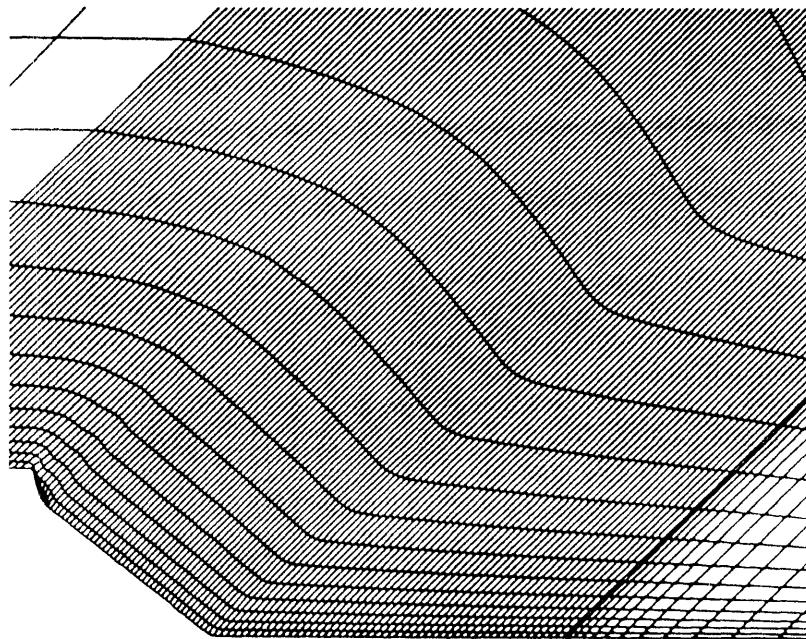
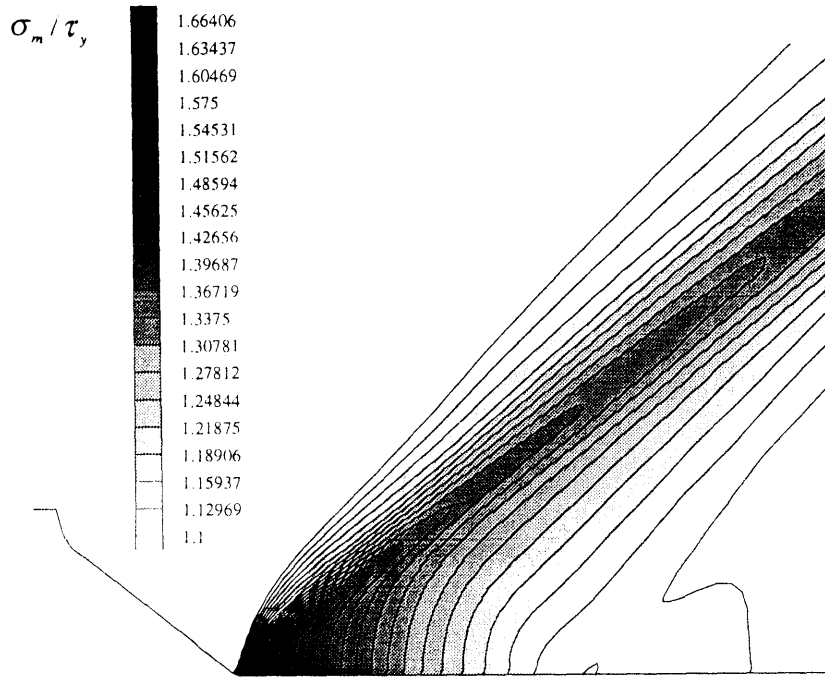


Fig. 4.10 (b) Stress triaxiality σ_m / τ_y contours near the crack-tip for $A=1.0$ and $(a-a_0)/l_0=0.16$ (top). Finite element mesh corresponding to the region of σ_m / τ_y contours (bottom).

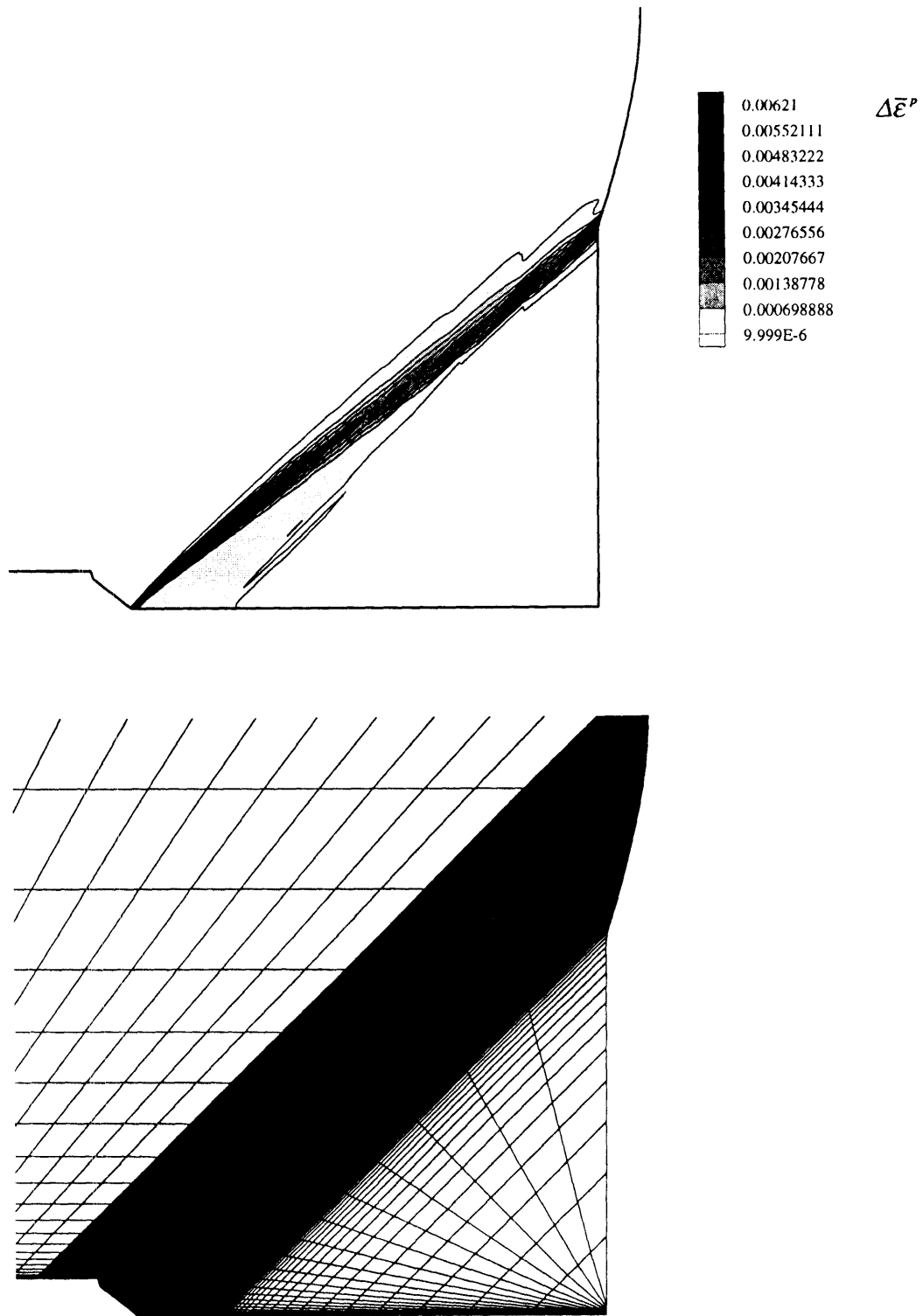


Fig. 4.11 (a) Incremental equivalent plastic strain $\Delta \bar{\epsilon}^p$ contours for $A = 1.0$ and $(a - a_0)/l_0 = 0.16$ (top). Finite element mesh corresponding to the region of $\Delta \bar{\epsilon}^p$ contours (bottom).

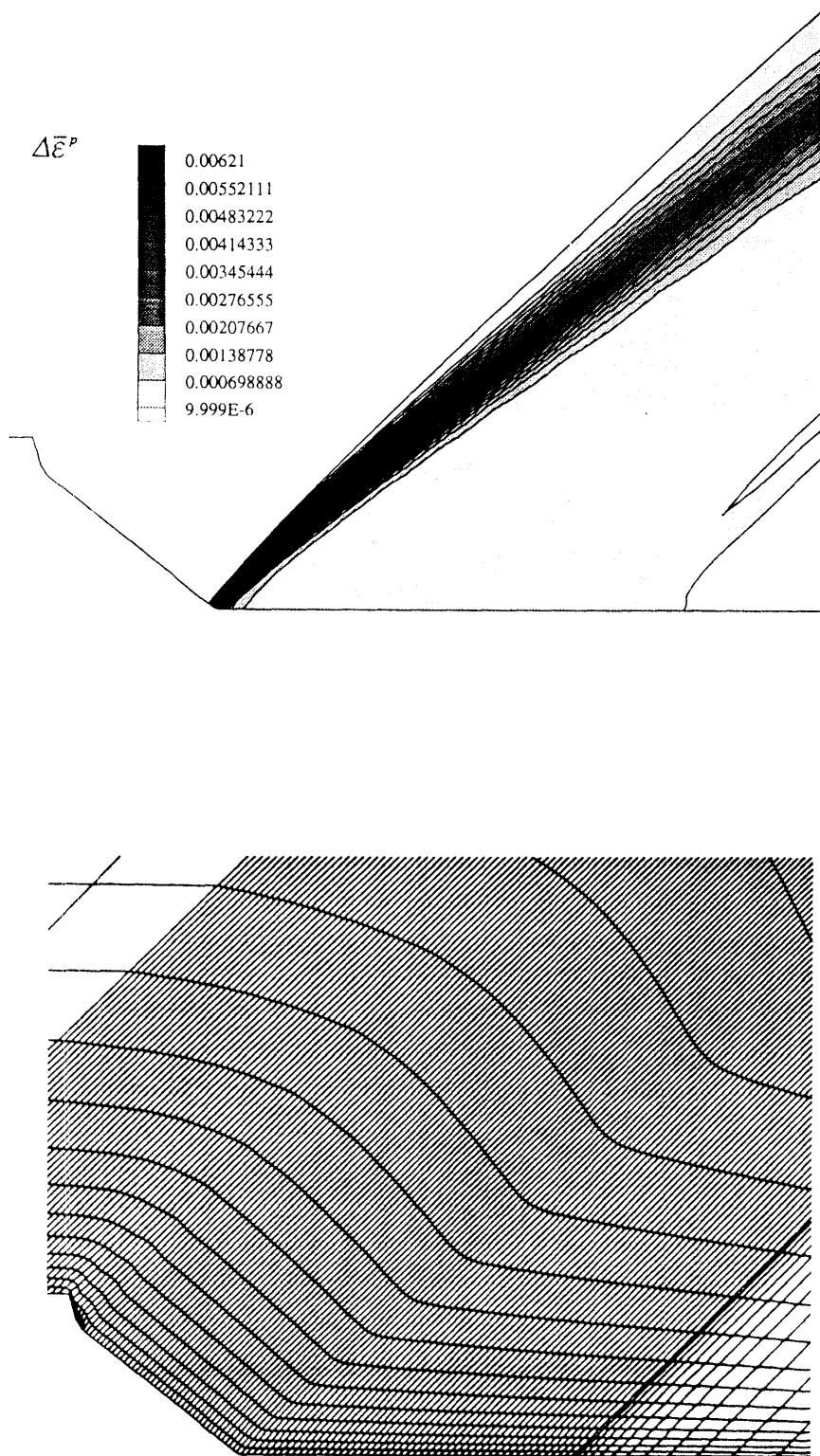


Fig. 4.11 (b) Incremental equivalent plastic strain $\Delta \bar{\epsilon}^p$ contours near the crack-tip for $A = 1.0$ and $(a - a_0)/l_0 = 0.16$ (top). Finite element mesh corresponding to the region of $\Delta \bar{\epsilon}^p$ contours (bottom).

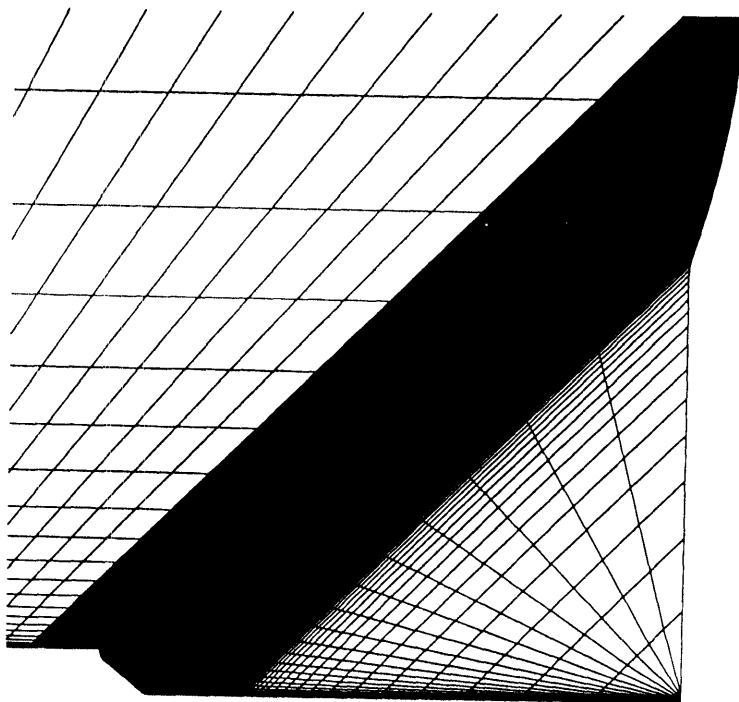
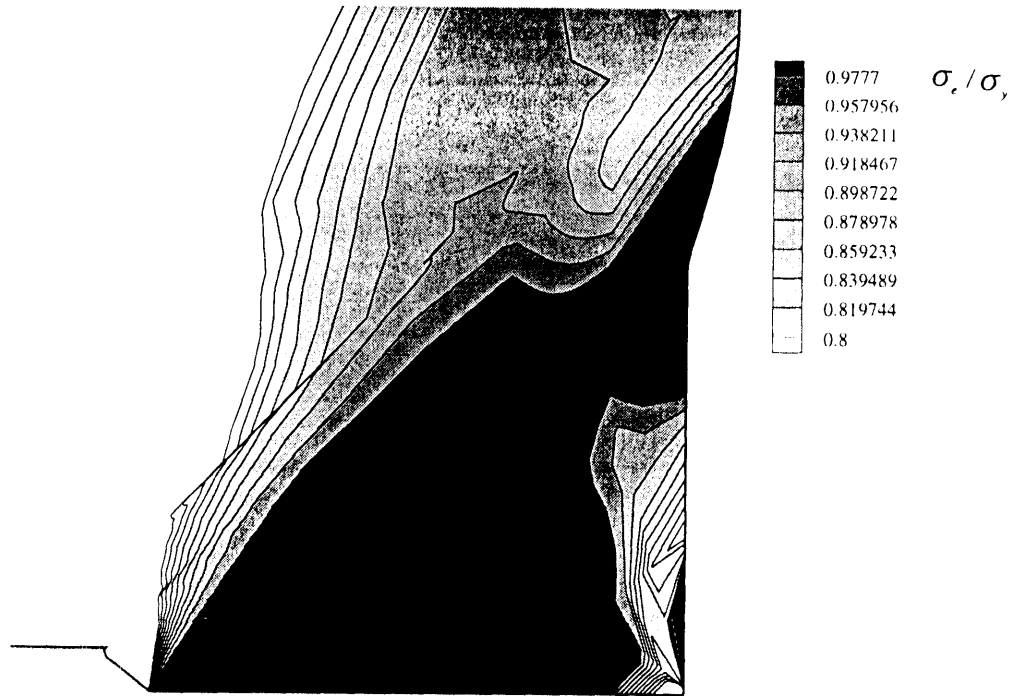


Fig. 4.12 Normalized Mises stress σ_c / σ_y contours for $A = 1.0$ and $(a - a_0) / l_0 = 0.16$ (top). Finite element mesh corresponding to the region of σ_c / σ_y contours (bottom).

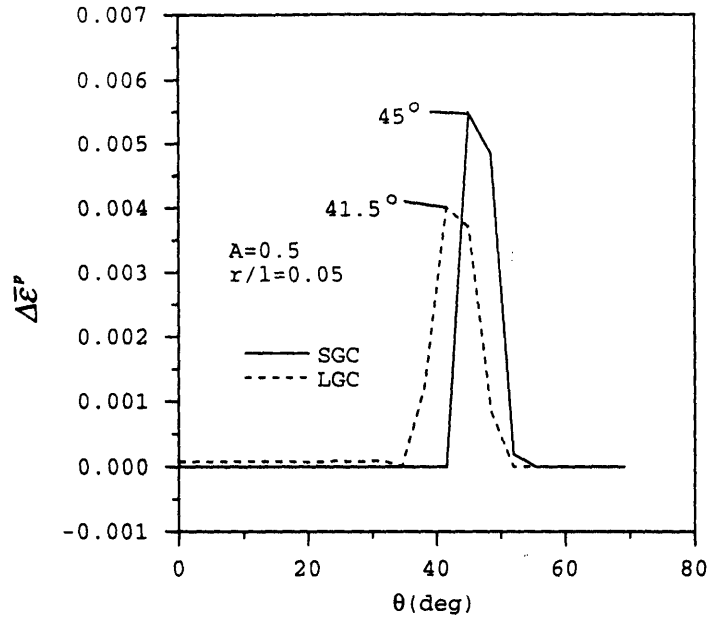


Fig. 4.13 (a) Incremental equivalent plastic strain $\Delta\bar{\epsilon}^P$ vs. θ plots obtained at $r = 5 \times 10^{-2}l$ for $A = 0.5$.

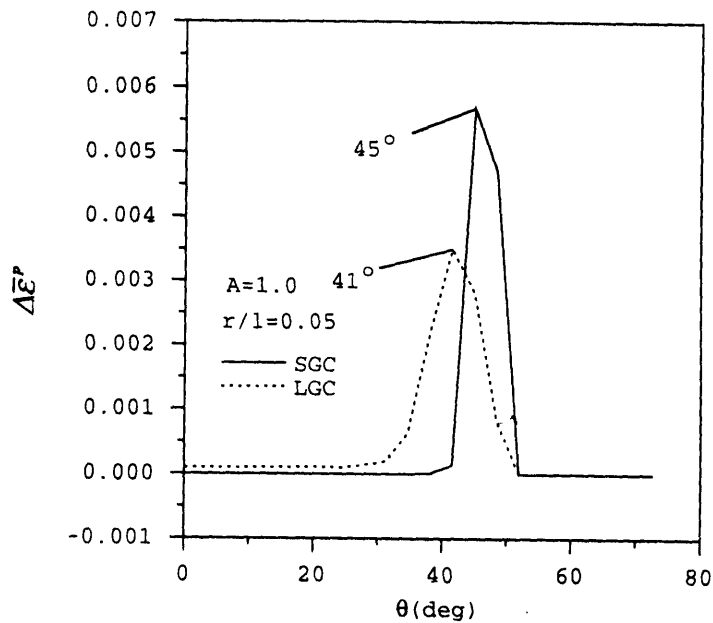


Fig. 4.13 (b) Incremental equivalent plastic strain $\Delta\bar{\epsilon}^P$ vs. θ plots obtained at $r = 5 \times 10^{-2}l$ for $A = 1.0$.

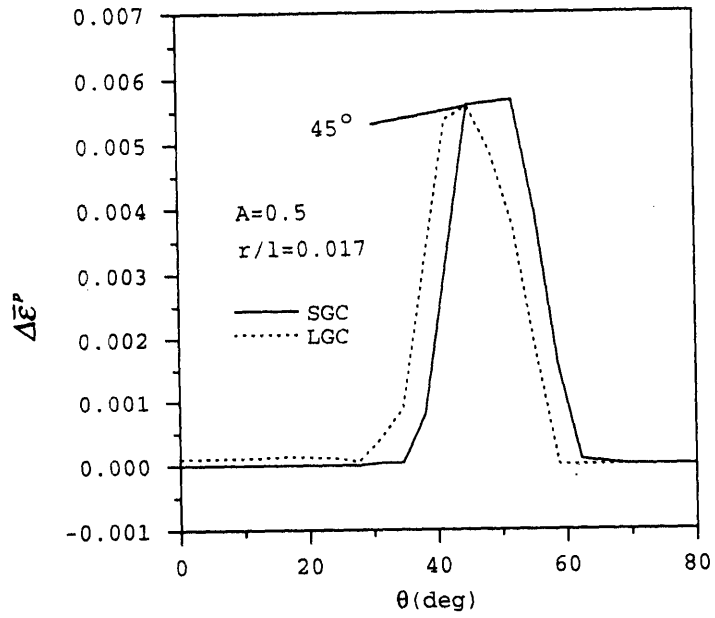


Fig. 4.14 (a) Incremental equivalent plastic strain $\Delta\bar{\epsilon}^p$ vs. θ plots obtained at $r = 1.7 \times 10^{-2}l$ for $A = 0.5$.

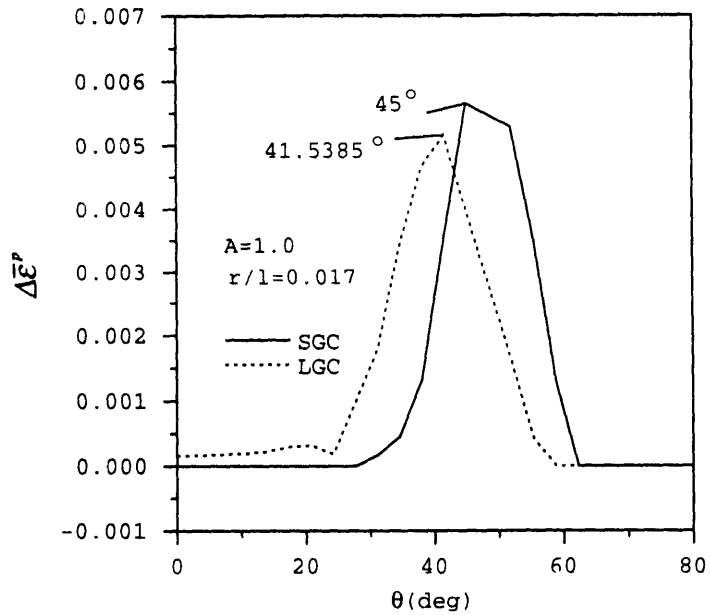


Fig. 4.14 (b) Incremental equivalent plastic strain $\Delta\bar{\epsilon}^p$ vs. θ plots obtained at $r = 1.7 \times 10^{-2}l$ for $A = 1.0$.

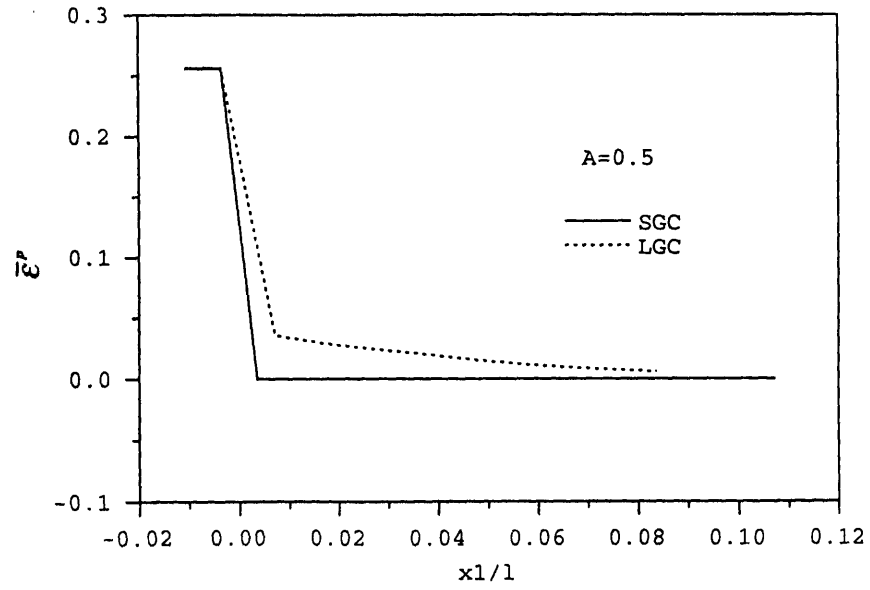


Fig. 4.15 (a) Equivalent plastic strain $\bar{\epsilon}^p$ vs. $x1/l$ for $A = 0.5$.

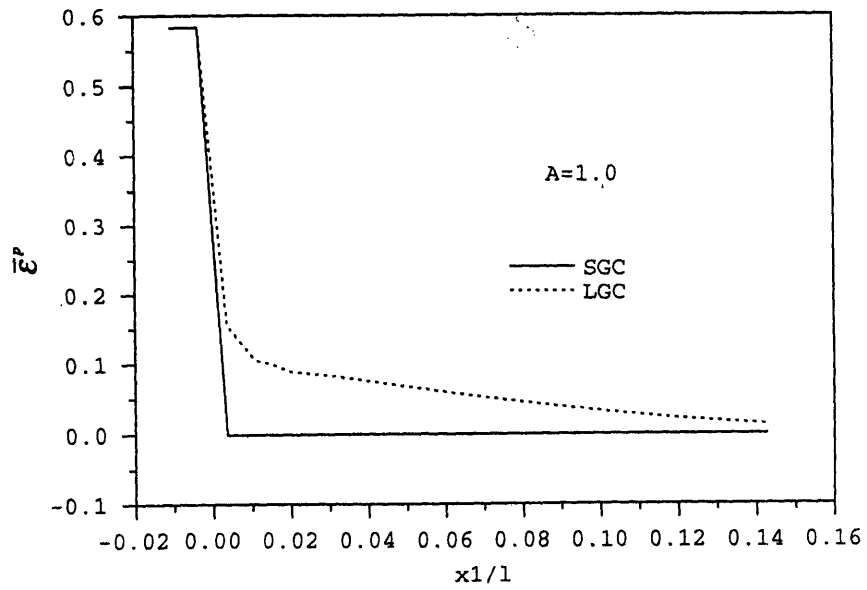
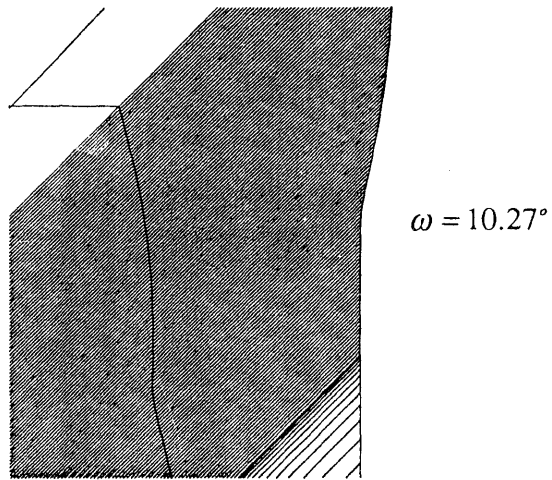
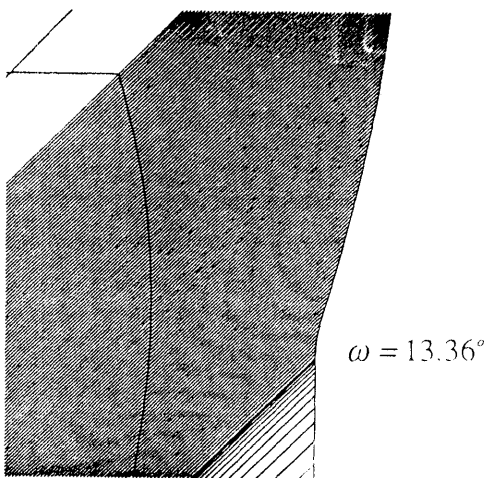


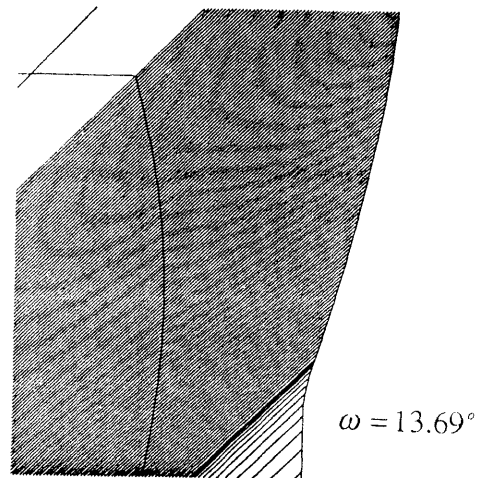
Fig. 4.15 (b) Equivalent plastic strain $\bar{\epsilon}^p$ vs. $x1/l$ for $A = 1.0$.



(a)



(b)



(c)

Fig. 4.16 Deformed mesh configurations showing backface angle ω at
 (a) $(a - a_o)/l_o = 0.045$, (b) $(a - a_o)/l_o = 0.11$, and (c) $(a - a_o)/l_o = 0.16$.

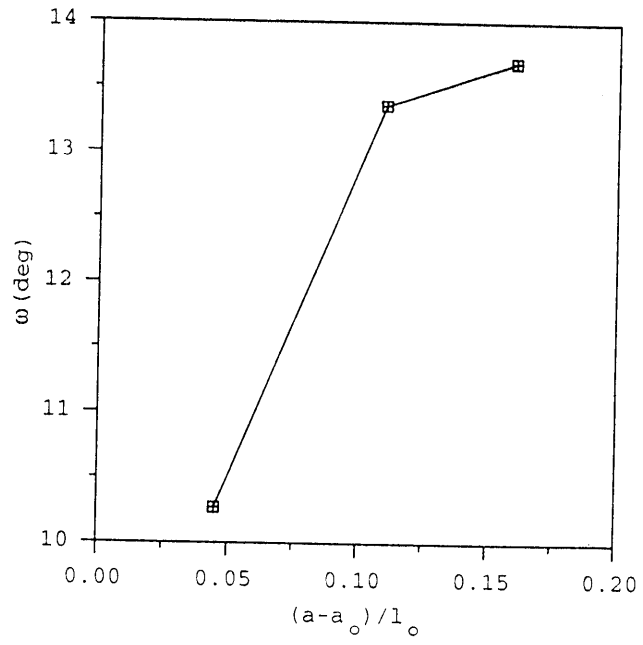


Fig. 4.17 Backface angle ω vs. crack extension $(a-a_0)/l_0$.

Chapter 5

Conclusion and Future work

5.1 Conclusion

In this work, fully plastic crack growth mechanics for low strength materials was explored using the present FEM/continuum model. A deeply-cracked single edge specimen composed of an isotropic elastic/perfectly plastic material was modeled. Here, the CTOA crack growth criterion (McClintock, et al., 1994) was adopted for fully plastic crack growth. First, small geometry change analyses were conducted in the present model to verify the consistency between the line-spring model formulations (Lee and Parks, 1994c) and the present model formulations. Choosing the highly refined and flow-line-oriented mesh configuration, the results (load-deflection curve) from the continuum model were found to be in good agreement with those of the line-spring model under pure extension.

The results show that the applied load decreases almost linearly with increasing far-field displacement immediately after crack initiation for both SGC analyses and LGC analyses. The increase of the ductility parameter A slows down the crack growth per unit imposed displacement. Soon after crack initiation, the loading geometry-based CTOA increases and saturates to a constant value. The load states under pure extension based on SGC analyses and LGC analyses are observed to be nearly similar.

The stress triaxiality at the crack in LGC analyses is observed to be higher than that in SGC during quasi-steady crack growth. Here, the new slip field with a centered fan is imposed to account for such crack-tip triaxiality elevation in LGC. The predictions based on the imposed slip line field show good agreement with the numerical results of LGC analyses.

5.2 Future work

Some feedback control algorithm based on the local geometry at the crack-tip may be needed in order to be able to implement the debonding curve associated with the relative displacement of the currently releasing node in order to remove a reloading process, which is a purely numerical effect.

The validity of the value of the strain hardening parameter, f , which Lee and Parks (1994c) chose for the line spring model for fully plastic crack growth in a low-hardening material, can be verified by comparing results from a strain hardening generalization of present FEM/continuum model.

The effects of geometry change on crack extension behavior under different loading conditions need to be studied. Under pure tension or pure bending, the stress triaxiality at the crack-tip is very high. Therefore, CTOA decreases to a minimum value for any given A immediately after crack initiation. Consequently, with a low value of CTOA (leading to small change of the backface angle), the geometry change effects are expected to be small compared to those under pure extension. Also, the geometry change effect in a low-hardening material needs to be studied.

Here, the inconsistency of the loading geometry-based CTOA with the crack-tip fields, is clearly addressed. Therefore, CTOA, which is chosen as a fracture criterion, needs to be more closely based on the information of the crack-tip field: The model may

need to be modified to obtain CTOA directly from the local geometry at the crack-tip using both (2.5) and (2.6) so that it can reflect the elevation of the crack-tip triaxiality. Such a microscopic approach to CTOA allows us to study the direct effect on the crack-tip field due to geometry change of the back face of a single edge specimen during crack growth. The increase of the crack-tip triaxiality due to the geometry change (an increase of back face angle) leads to a decrease of CTOA, which in turn results in the decrease of the back face angle, thus coupling geometry change with CTOA. It will be interesting to determine whether a coupling with geometry change allows the deformation field near the growing crack-tip to converge to steady state, which has been observed in the previous numerical studies for stable crack growth (Rice and Sorenson, 1978; Drugan, et al., 1982).

Another issue of interest is the effect of the deformation-induced geometry change on the accuracy of the proposed m -family solutions for the growing crack under large scale yielding and general yielding (Drugan and Chen, 1989; Chen and Drugan, 1991; Liu and Drugan, 1993), which were developed under small geometry change.

References

- Anderson, H., 1973, "A Finite Element Representation of Stable Crack Growth," *Journal of the Mechanics and Physics of Solids*, Vol. 21, pp. 337-356
- Al-Ani, A. M. and Hancock, J. W., 1991, "J - Dominance of Short Cracks in Tension and Bending," *Journal of the Mechanics and Physics of Solids*, Vol. 39, pp. 23-43.
- Betegon, C. and Hancock, J. W., 1991, "Two Parameter Characterization of Elastic-Plastic Crack-Tip Fields," *Journal of Applied Mechanics*, Vol. 58, pp. 104-110.
- Bilby, B. A., Cardew, G. E., Goldthorpe, M. R. and Howard, I. C., 1986, "A Finite Element Investigation of the Effect of Specimen Geometry on the fields of stress and strain at the Tip of stationary Cracks," in *Size effects in Fracture*, I. Mech. E., London, pp. 37-46.
- Bishop, J. F. W., and Hill, R., 1951, A theory of the plastic distortion of a polycrystalline aggregate under combined stresses. *Phil. Mag.* 42, 414-427
- Carson, J. W., 1970, "A study of Plane Strain Ductile Fracture," Ph.D. Thesis, Department of Mechanical Engineering, Massachusetts Institute of Technology.
- Chakrabarty, J., 1987, *Theory of Plasticity*, McGraw-Hill, New York.
- Chen, X., and Drugan, W. J., 1991, "Plane Strain Elastic-Ideally Plastic Crack Fields for Mode I Quasistatic Growth at Large-Scale Yielding--II. Global Analytical Solutions for Finite Geometries," *Journal of the Mechanics and Physics of Solids*, Vol. 39, pp. 895-925.
- Drugan, W. J., Rice, J. R. and Sham, T.-L., 1982, "Asymptotic Analysis of Growing Plane Strain Tensile Cracks in Elastic-Ideally Plastic Solids," *Journal of the Mechanics and Physics of Solids*, Vol. 30, pp. 447-473.
- Drugan, W. J., and Chen, X., 1989, "Plane Strain Elastic-Ideally Plastic Crack Fields for Mode I Quasistatic Growth at Large-Scale Yielding--I. A New Family of Analytical Solutions," *Journal of the Mechanics and Physics of Solids*, Vol. 37, pp. 1-26.
- Gudmundson, P., 1989, "Validity of Asymptotic Crack Tip Solutions for Plastic Materials," in *Advances in Fracture Research*, Vol. 1, Proceedings of the 7th International Conference on Fracture, Salama K. et al., Houston, U.S.A., pp. 315-322.
- Gurson, A. L., 1977, "Continuum theory of ductile rupture by void nucleation and growth: Part I -Yield criteria and Flow Rules for Porous Ductile Media," *Journal of Engineering Materials and Technology*, Vol. 99, pp. 2-15.
- Green, A. P. and Hundy, B. B., 1956, "Initial Plastic Yielding in Notch Bend Tests," *Journal of the Mechanics and Physics of Solids*, Vol. 4, pp. 128-144.

Hancock, J. W., Reuter, W. G., and Parks, D. M., **1993**, "Constraint and Toughness Parameterized by T," in *Constraint Effects in Fracture*, ASTM STP 1171, E. M. Hackett, K.-H. Schwalbe and R. H. Dodds, Jr., Eds., American Society for Testing and Materials, Philadelphia pp. 21-40.

Hibbitt, Karlsson and Sorenson, Inc., **1994**, *ABAQUS User's Manual*, version 5.3, Hibbitt, Karlsson and Sorenson, Inc., Providence, RI.

Hutchinson, J. W., **1968**, "Singular Behavior at the End of a Tensile Crack in a Hardening material," *Journal of the Mechanics and Physics of Solids*, Vol. 16, pp. 13-31.

Kim, Y.-J., McClintock, F. A. and Parks, D. M., **1994a**, "Global Equilibrium of the Least Upper Bound Circular Arc and its Application to Fracture Mechanics," submitted to *Mechanics of Materials*.

Kannien, M. F., Rybicki, E. F., Stonesifer, R. B., Broek, D., Rosenfield, A., Marshall, C. W. and Hahn, G. T., **1979**, "Elastic-plastic fracture mechanics for two dimensional stable crack growth and instability problems," In *Elastic-Plastic Fracture*, ASTM STP 668 (eds. J. D. Landes, J. A. Begley and G. A. Clarke) American Society for Testing Materials, Philadelphia, 121-150.

Kim, Y.-J., McClintock, F. A. and Parks, D. M., **1994b**, "Yield Locus in Deep, Single Face Cracked Specimens Under Combined Bending and Tension," accepted for publications as Brief note, *Journal of Applied Mechanics*.

Kim, Y.-J., McClintock, F. A. and Parks, D. M., **1994c**, "Line-Spring Model for Fully Plastic, Plane Strain Crack Growth in Plates and Shells," submitted to *International Journal of Fracture*.

Larsson, S. G. and Carlsson, A. J., **1973**, "Influence of Non-singular Stress Terms and Specimen Geometry on Small-Scale Yielding at Crack Tips in Elastic-Plastic Material," *Journal of the Mechanics and Physics of Solids*, Vol. 21, pp. 263-277.

Lee, H. and Parks, D. M., **1993**, "Fully Plastic Analyses of Plane Analyses of Plane Strain Single Edge Specimens Subject to Combined Tension and Bending," *International Journal of Fracture*, Vol. 63, pp. 329-349.

Lee, H. and Parks, D. M., **1994a**, "Enhanced Elastic-Plastic Line-Spring Finite Elements," *International Journal of Solid and Structure*, in press.

Lee, H. and Parks, D. M., **1994b**, "Line-Spring Finite Element for Fully Plastic Crack Growth," submitted to *International Journal of Solid and Structure*.

Liu, N. and Drugan, W. J., **1993**, "Finite -element Solutions of Crack-growth in incompressible Elastic-plastic Solids with Various Yielding extents and loadings: Detailed Computations with Analytic Solutions", *International Journal of Fracture*, Vol. 59, pp. 265-289.

McClintock, F. A., **1969**, "Crack Growth in Fully Plastic Grooved Tensile Specimens," in *Physics of Strength and Plasticity: Orowan Anniversary Volume*, Argon, A.S., Ed., MIT Press, Cambridge, pp. 307-326.

McClintock, F. A., Kim, Y.-J. and Parks, D.M., **1994**, "Criteria for Plane Strain, Fully Plastic Quasi-steady Crack Growth," accepted for publication, *International Journal of Fracture* .

McClintock, F. A., Kim, Y.-J. and Parks, D. M., **1995**, "Tests and Analyses for Fully Plastic Fracture Mechanics of Plane Strain Mode I Crack Growth," In *Fracture Mechanics, ASTM STP 668* (eds. Walter G. Reuter, John H. Underwood, and James C. Newman) American Society for Testing Materials, Philadelphia.

O'Dowd, N. P. and Shih, S. F., **1992**, "Family of Crack-Tip Fields Characterized by a Triaxiality Parameter: Part II - Fracture Applications," *Journal of the Mechanics and Physics of Solids*, Vol. 40, pp. 939-963

Rice, J. R. and Rosengren, G. F.,**1968**, "Plane Strain Deformation Near a Crack Tip in a Power Law Hardening Material," *Journal of the Mechanics and Physics of Solids*, Vol. 16, pp. 1-12.

Rice, J. R. and Sorenson, E. P., **1978**, "Continuing Crack-Tip Deformation and Fracture for Plane-Strain Crack Growth in Elastic-Plastic Solids," *Journal of the Mechanics and Physics of Solids*, Vol. 26, pp. 163-186.

Shih, C.F., deLorenzi, H.G. and Andrews, W. R. **1979**, "Studies on crack initiation and stable crack growth," In *Elastic-Plastic Fracture, ASTM STP 668* (eds. J.D. Landes, J.A. Begley and G.A. Clarke) American Society for Testing Materials, Philadelphia, 65-120.

Tvergaard, V. and Needleman, A., **1992**, "Effect of Crack Meandering on Dynamic, Ductile Fracture," *Journal of the Mechanics and Physics of Solids*, 40, 447-471

Williams, M. L., **1957**, "On the Stress Distribution at the Base of a Stationary Crack," *Journal of Applied Mechanics*, Vol. 24, pp. 111-114.

Xia, L., Shih, F., and Hutchinson, J. W., **1995**, "A Computational Approach to Ductile Crack Growth under Large Scale Yielding Conditions," *Journal of the Mechanics and Physics of Solids*, Vol. 43, pp. 389-413.